nature communications

Article

https://doi.org/10.1038/s41467-025-58124-7

Programmed enhancement of endogenous iron-mediated lysosomal membrane permeabilization for tumor ferroptosis/pyroptosis dual-induction

Received: 11 September 2024

Accepted: 11 March 2025

Published online: 28 March 2025

Check for updates

Luwen Zhu[1,2], Jiahao Hu[2], Xiaochuan Wu[2], Jucong Zhang[2], Xinyi Xu[2], Xiajie Huang[2], Bing Tian[3] ✉, Chun-Xia Zhao[4] ✉, Yongzhong Du[1,2] ✉ & Liming Wu[1] ✉

Ferroptosis and pyroptosis, as emerging regulated forms of cell death capable of overcoming apoptotic resistance, demonstrate promising potential in tumor therapy. Given that iron manipulation and reactive oxygen species elevation serve as common stimuli for both processes, inducing lysosomal membrane permeabilization (LMP) with ensuing release of lysosomal contents (including iron ions and cathepsins) is anticipated to realize dual induction of ferroptosis/pyroptosis. Herein, we report a folic acid and croconaine molecule-functionalized upconversion nanoparticle (UCNP-Cro/FA) that is able to mobilize intracellular stores of endogenous iron and spatiotemporally control the lysosome-intrinsic Fenton chemistry, thereby triggering LMP-associated cell death. The process of endogenous iron mobilization occurs through two key steps: Cro-mediated coordination of abundant Fe^{3+} ions within lysosomes, followed by UV-emitting upconversion core-mediated photoreduction, resulting in Fe^{2+} ions release. Both in vitro and in vivo experiments show that UCNP-Cro/FA + NIR treatment effectively boost LMP by endogenous iron-mediated •OH production, ultimately triggering irreversible tumor cell death via ferroptosis and Caspase-1/GSDMD-dependent pyroptosis pathways. Moreover, this process potentiates tumor immunogenicity, holding promise for tumor immunotherapy. Overall, this work proposes a feasible tumor therapy strategy that integrates ferroptosis and pyroptosis through the efficient application and activation of endogenous iron.

Surgery and chemotherapy are the primary clinical treatments for breast cancer, which is the second leading cause of death among women worldwide[1,2]. However, neither achieves desirable therapeutic outcomes: surgery can inadvertently promote the growth of metastases, while chemotherapy often induces severe side effects and contributes to apoptotic resistance in cancer cells[3,4]. Therefore, research on the establishment of an alternative therapeutic modality to induce other non-apoptotic cell death holds promise for effective antitumor treatment.

[1]Department of General Surgery, Center for Metabolism Research, The Fourth Affiliated Hospital of School of Medicine and International School of Medicine, International Institutes of Medicine, Zhejiang University, Yiwu 322000, P. R. China. [2]State Key Laboratory of Advanced Drug Delivery and Release Systems, Institute of Pharmaceutics, College of Pharmaceutical Sciences, Zhejiang University, Hangzhou 310058, P. R. China. [3]Institute of Biophysics, College of Life Sciences, Zhejiang University, Hangzhou, Zhejiang 310058, P. R. China. [4]School of Chemical Engineering, The University of Adelaide, Adelaide, SA, Australia. ✉e-mail: tianbing@zju.edu.cn; chunxia.zhao@adelaide.edu.au; duyongzhong@zju.edu.cn; wlm@zju.edu.cn

In recent years, multiple novel forms of regulated cell death, such as ferroptosis, pyroptosis, and cuproptosis, have been discovered and characterized with their corresponding molecular mechanisms[5–7]. Among these, the elevated intracellular iron and reactive oxygen species (ROS) levels have been recognized as common stimuli for both ferroptosis and pyroptosis[8,9]. Specifically, ferroptosis occurs via iron-catalyzed lipid peroxidation, and pyroptosis is an inflammatory cell death process that can also be triggered by iron-activated ROS signaling[10–12]. As a result, inducing intracellular iron overload has the potential to simultaneously initiate both forms of cell death, thereby amplifying the therapeutic effect.

With the rapid development of nanotechnology, various iron-based functionalized nanomaterials such as iron oxide nanoparticles[13], iron-organic frameworks[14], and amorphous iron nanoparticles (AFeNPs)[15] have received much attention in antitumor therapy owing to their capacity to deliver exogenous iron into cells. However, considering the low efficiency of iron release from these iron-based materials, an excessive dose is required to achieve the desired therapeutic effect, which may cause potential adverse effects on human health, increasing the risk of various acute and chronic toxicities[16–18]. Therefore, besides the introduction of external iron sources, harnessing plentiful and safe endogenous iron sources may be a superior alternative. Lysosomes are important iron storage hubs, which govern the homeostatic turnover of iron-containing proteins, such as transferrin and ferritin[19]. To date, many molecules such as siramesine and salinomycin, or nanoplatforms with lysosomal membrane destruction ability, have been developed to induce lysosomal membrane permeabilization (LMP), realizing the efficient release of lysosomal iron[20–23]. It was noteworthy that apart from iron, various hydrolases (e.g., cathepsin B) would also spill out of lysosomal lumen into the cytosol during LMP[24]. As an upstream initiation signaling of the nucleotide-binding oligomerization domain-like receptor protein 3 (NLRP3) inflammasome, cathepsin B has been demonstrated to activate caspase-1 dependent pyroptosis[25,26]. In this situation, leaky and ruptured lysosomes are considered bombs that can trigger cell ferroptosis and pyroptosis by releasing self-killing endogenous substances.

In this work, we develop a Tm^{3+}-Yb^{3+} codoped up-conversion nanoparticle functionalized with folic acid and croconaine molecules (UCNP-Cro/FA), which can enhance the retention of iron within lysosomes prior to its mobilization and release, thereby amplifying LMP-associated cell death. As a prerequisite for subsequent cascade reactions, the UCNP-Cro/FA nanoparticles target tumor cells through specific binding with folate receptor (FR) overexpressed on the surface of tumor cells, and rapidly concentrate in lysosomes via FR-mediated endocytic pathway. Sequentially, the croconaine molecules (Cro) allow for coordinating with abundant Fe^{3+} ions in lysosomes so as to block the translocation of iron into the cytosol. In response to the ensuing cytoplasmic depletion of iron, cells initiate the lysosomal degradation of ferritin, further facilitating the loading of endogenous iron in lysosomes. Upon near-infrared (NIR) irradiation, the ultraviolet (UV) emitting from upconversion core realize the valence conversion of iron ions, resulting in the liberation of Fe^{2+} ions. Benefit from the deficient catalase and low acidic environment in lysosomes, the redox-active Fe^{2+} ions can effectively catalyze hydrogen peroxide (H_2O_2) into highly toxic hydroxyl radicals (•OH) via the Fenton reaction without being scavenged, leading to lysosomal membrane rupture and the outflow of lysosomal contents (including iron ions and cathepsin B). After that, this study delves into the detailed cell death pathways of UCNP-Cro/FA upon NIR irradiation treatment. Surprisingly and excitingly, our results demonstrate that the treatment triggered irreversible tumor cell death via ferroptosis and Caspase-1/GSDMD-dependent pyroptosis in vitro, and markedly inhibit tumor growth in vivo. Given the feasibility of achieving dual induction of ferroptosis and pyroptosis through the programmed enhancement of endogenous iron-mediated lysosomal dysfunction, this research provides potential insights for designing safe and effective antitumor nanotherapies (Fig. 1).

Results

Synthesis and Characterization of UCNP-Cro/FA

First, the croconaine molecules containing carboxyl groups (denoted as Cro) were synthesized following the procedure shown in Supplementary Fig. 1. The chemical structures of the intermediates and Cro were validated by ^1H nuclear magnetic resonance (NMR) and mass spectrometry (MS; Supplementary Figs. 2–5). Analysis of the UV absorption spectrum of Cro revealed a maximum absorption peak at 804 nm, with absorbance at this wavelength showing a positive correlation with its concentration (Supplementary Fig. 6).

Subsequently, the folic acid (FA) and croconaine molecule-functionalized upconversion nanoparticles (UCNP-Cro/FA) were fabricated through a three-step process delineated in Supplementary Fig. 7, encompassing the synthesis of hydrophilic NaYF4: Yb^{3+}, Tm^{3+} UCNP, the amination of UCNP, and the covalent coupling of NH_2-functionalized UCNP with carboxyl-containing molecules.

Specifically, hydrophobic oleic-acid-capped upconversion nanoparticles (UCNP-OA) were synthesized following previously reported methods[27]. Transmission electron microscopy (TEM) image showed that the as-obtained particles were uniform with a diameter of 50 nm (Supplementary Fig. 8). X-ray diffraction (XRD) analysis revealed that all the diffraction peaks of UCNP-OA coincided well with the pure hexagonal phase of the $NaYF_4$ standard pattern (JCPDS 16-0334), which was consistent with the crystal structures observed in the TEM image (Supplementary Fig. 9). Moreover, energy-dispersive X-ray spectroscopy (EDS) demonstrated the presence of template ions (F^-, Na^+, and Y^{3+}) and rare-earth dopant ions (Yb^{3+} and Tm^{3+}) (Fig. 2A). Under continuous irradiation of a 980 nm laser, UCNP-OA demonstrated upconversion luminescence (UCL) spectra featuring distinct ultraviolet and blue emission bands arising from Tm transitions: $^1I_6 \rightarrow {}^3F4$, $^1D_2 \rightarrow {}^3H_6$ (347, 363 nm) and $^1D_2 \rightarrow {}^3F_4$, $^1G_4 \rightarrow {}^3H_6$ (452, 475 nm) (Supplementary Fig. 10). These results confirmed the successful preparation of NaYF4: Yb^{3+}, Tm^{3+} UCNP.

The hydrophobic upconversion nanoparticles were then made water-dispersible and amine-functionalized by a ligand exchange process utilizing 2-aminoethyl dihydrogen phosphate (AEP) as a surface-coating agent to replace the original OA ligands. The success of hydrophilic exchange was evidenced by the emergence of characteristic absorption bands assigned to AEP (such as P-O-C at 1109 cm^{-1} and O = P at 1638 cm^{-1}), along with the vanishing of OA-associated absorption bands (such as -COO- at 1542 cm^{-1}, 1459 cm^{-1}, and the long alkyl chain (-CH2-, $n > 4$) at 2923 cm^{-1}) in the Fourier transform infrared (FTIR) spectra (Fig. 2B). The fluorescamine assay revealed that the as-synthesized UCNP-NH_2 possessed an amino content of ~150 nmol per mg (Supplementary Fig. 11), thereby facilitating its subsequent covalent conjugation with carboxyl-terminated molecules (FA-PEG-COOH and Cro) to obtain UCNP-Cro/FA. As shown in Fig. 2C and Supplementary Fig. 12, the UV-Vis and FT-IR spectra exhibited discernible peaks corresponding to Cro and FA-PEG in UCNP-Cro/FA, providing evidence for the covalent functionalization of UCNP-NH_2. And the amount of Cro conjugated to UCNP-NH_2 was 3.11% wt, as determined from the UV-Vis spectra. Additionally, the charge of UCNP-Cro/FA underwent a shift toward negative values (-11.5 ± 0.17 mV) in contrast to the positive charge observed for UCNP-NH_2 (+23.4 ± 0.94 mV), which was ascribed to the presence of conjugated Cro and FA on the surface (Fig. 2G). Due to the small molecular weight of conjugated molecules, no substantial change was noted in the particle size of UCNPs before and after modification. And the TEM images presented in Fig. 2E, F indicated that UCNP-Cro/FA displayed an analogous morphology and high monodispersity to UCNP-NH_2. Notably, under NIR irradiation (980 nm, 1.0 W/cm^2), all the UCNP aqueous dispersion samples exhibited intense UV light emission, with peak wavelengths

ranging from 340 nm to 360 nm (Figs. 2D and Supplementary Fig. 13), suggesting that surface modification minimally altered the optical properties of the nanoparticles. Additionally, Endotoxin testing (Supplementary Table 1) indicated that UCNP-Cro/FA dispersion was endotoxin-free, with levels below the 0.01 EU/mL detection threshold, ensuring a contaminant-free basis for subsequent in vitro and in vivo assessments.

Cro-mediated coordination of Fe^{3+} and NIR-triggered release of reduced Fe^{2+}

Given the documented capacity of Cro molecules for reversible binding with iron in applications such as colorimetric fluorescence sensing[28], we sought to elucidate the coordination proficiency of UCNP-Cro/FA nanoparticles in this regard. To this end, Fe^{3+} ions were introduced into the UCNP-Cro/FA solution. Subsequent observations unveiled a gradual decrease in both the fluorescence intensity and absorbance at 804 nm of the Cro molecules conjugated onto the UCNP-Cro/FA nanoparticles as the concentration of Fe^{3+} ions increased (Fig. 2H, I). According to the Hard and Soft Acid-Base (HSAB) principle, this phenomenon arose from the hard-hard interaction between Fe^{3+} ions and Cro molecules, indicating the formation of Cro–Fe complexes.

Notably, previous studies have shown that upon reduction of Fe^{3+} to Fe^{2+}, the poor binding strength between Fe^{2+} ions and Cro typically leads to the disintegration of the coordination bond, thereby facilitating the regeneration of Cro[29,30]. Meanwhile, it has been reported that UV light can catalyze the reduction of Fe^{3+} to Fe^{2+} through a photochemically induced electron transfer mechanism from a complexing organic ligand to an oxidized metal species[31–34]. In this case, we were intrigued by the potential of UCNP, leveraging its capacity for NIR to UV conversion, to enable the valence transformation from Fe^{3+} to Fe^{2+} and the disruption of coordination bond between Cro and iron. For verification, the evolution of Fe^{3+} ions under 980 nm NIR irradiation subsequent to its coordination with UCNP-Cro/FA nanoparticles was evaluated using 1,10-phenanthroline, a compound capable of reacting with reduced Fe^{2+} ions to form a stable purple complex. As shown in Fig. 2J, K, the absorption intensity of the supernatant at 510 nm following exposure to both UV and NIR irradiation exhibited a pronounced elevation compared to that non-irradiated. Moreover, the absorption intensity gradually increased with NIR irradiation time. These observations provided evidence that the UV light emitted by the UCNP-Cro/FA nanoparticles could efficiently transform Fe^{3+} into Fe^{2+}, thereby eliciting the release of Fe^{2+} ions. As expected, we noted that the absorption peak and fluorescence of UCNP-Cro/FA nanoparticles that had disappeared due to the coordination with Fe^{3+} ions were restored under NIR irradiation (Fig. 2L and Supplementary Fig. 14), while exposure Cro–Fe complexes to NIR light in the absence of UCNP did not, further substantiating the necessity of UCNP-mediated photon upconversion process for the photoreduction of Fe^{3+} ions. In short, the UCNP-Cro/FA nanoparticles exhibited a notable capacity for Fe^{3+} ions chelation, resulting in the quenching of UV absorbance and fluorescence, thereby establishing an "off" state. However, upon NIR irradiation, the coordination bond underwent cleavage, facilitating the restoration of the above characteristics and effectuating the transition

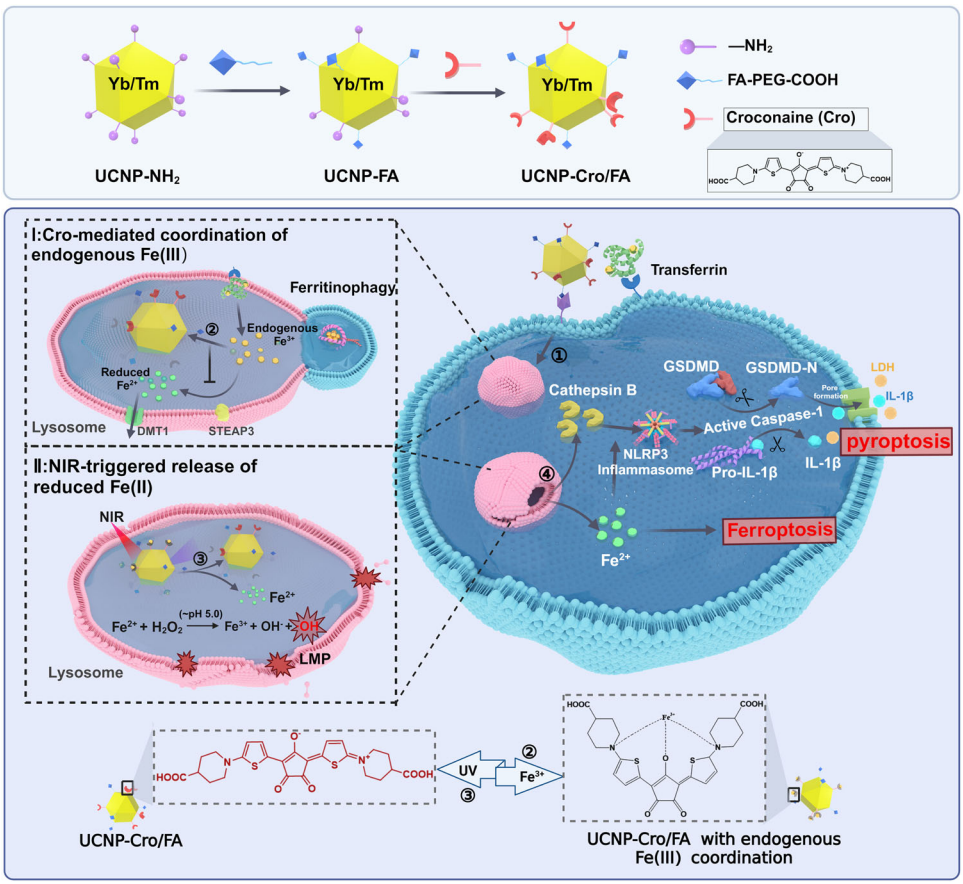

Fig. 1 | Schematic construction of UCNP-Cro/FA and its theranostic application. Schematic illustration of the synthetic procedure of the folic acid and croconaine molecule-functionalized upconversion nanoparticles (UCNP-Cro/FA) and its corresponding antitumor therapy. ① Folate receptor-mediated endocytosis and lysosomal accumulation of the nanoparticles. ② The coordination of the nanoparticles with Fe^{3+} ions in lysosomes. ③ UV-assisted Fe^{3+}-to-Fe^{2+} conversion reinforced the Fenton reaction. ④ The generated •OH attacked the lysosomal membranes, causing content leakage and subsequently inducing ferroptosis and pyroptosis pathways. Created in BioRender. Luwen, Z. (2025) BioRender.com/s70z201.

https://doi.org/10.1038/s41467-025-58124-7

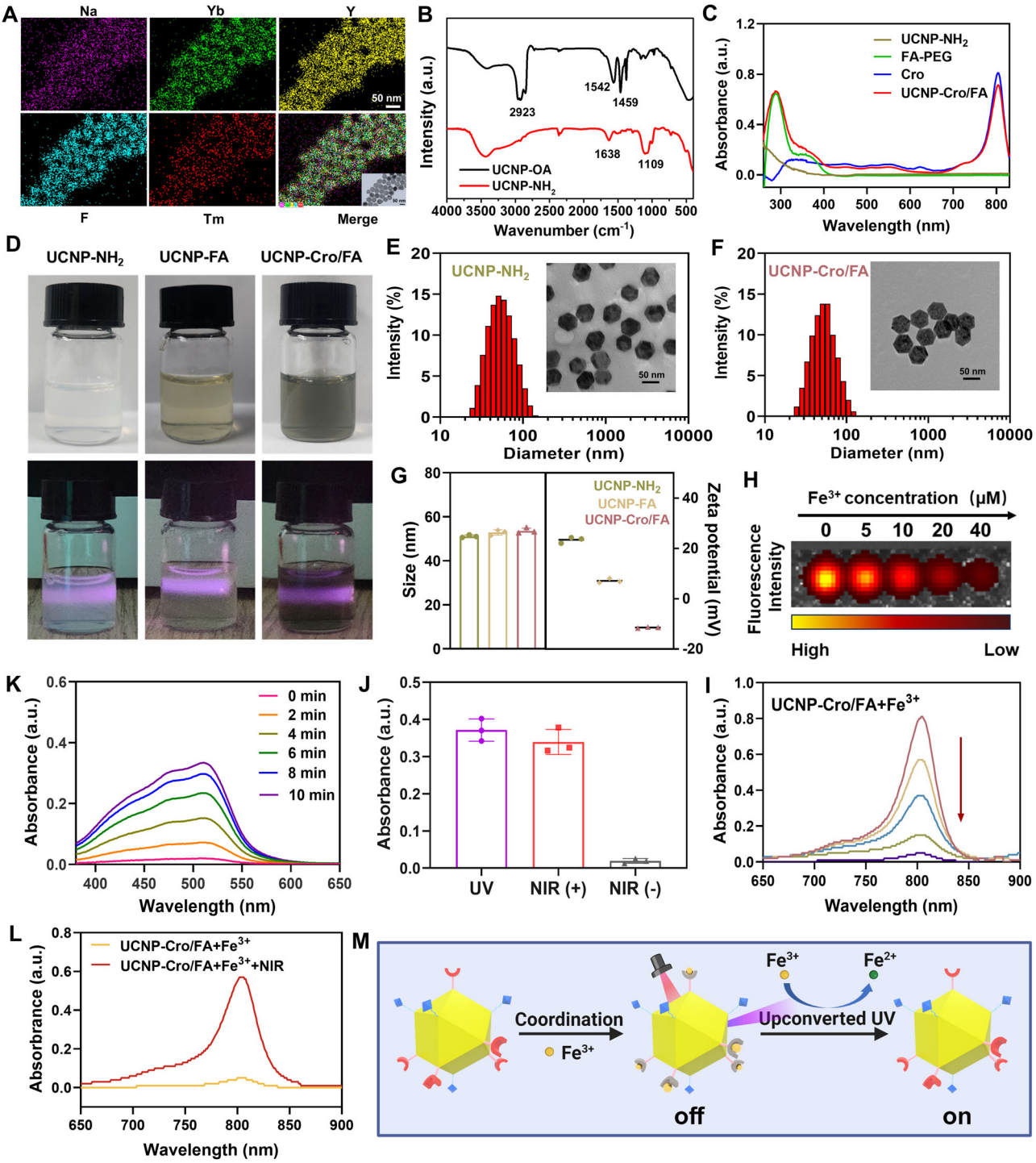

Fig. 2 | Preparation and characterization of UCNP-Cro/FA. A Element mapping images of UCNP-OA. **B** FTIR spectra of UCNP-OA and UCNP-NH_2. **C** UV–vis absorption spectra of UCNP-NH_2, Cro, FA-PEG, and UCNP-Cro/FA. UCNP-Cro/FA exhibited absorption peaks corresponding to FA-PEG at 284 nm and Cro at 804 nm. **D** Digital photograph of UCNP-NH_2, UCNP-FA, and UCNP-Cro/FA in aqueous solution with or without NIR irradiation. **E**, **F** Size distribution of UCNP-NH_2 and UCNP-Cro/FA in aqueous solution examined by DLS and TEM. **G** Comparison of size and zeta potential of different nanoformulations ($n = 3$ independent experiments in each group). **H** Fluorescence imaging of UCNP-Cro/FA solutions after incubation with various concentrations of Fe^{3+} ions. Ex/Em=780 nm/820 nm. **I** UV–Vis absorbance spectra of UCNP-Cro/FA solution with the addition of Fe^{3+} ions at different concentrations. **J** The absorbance of 1,10-phenanthroline-ferrous iron at 510 nm after different treatments of UCNP-Cro/FA + Fe^{3+} ions solution. UV and NIR lasers induced the valence conversion of Fe^{3+} ions in solution, indicating the photo-reduction of Fe^{3+} ions by UV irradiation ($n = 3$ independent experiments in each group). **K** UV–vis absorption spectra of 1,10-phenanthroline-ferrous iron in UCNP-Cro/FA + Fe^{3+} ions solution under 980 nm NIR irradiation for different times, showing the time-dependent production of Fe^{2+} ions. **L** Variation of UCNP-Cro/FA + Fe^{3+} ions solution absorption spectra with 980 nm NIR irradiation. M) Schematic illustration of UCNP-Cro/FA in response to Fe^{3+} ions and NIR light irradiation. Created in BioRender. Luwen, Z. (2025) BioRender.com/n85y153. Experiments in (**A**), (**D**), (**E**), (**F**) and (**H**) were repeated three times independently with similar results. Error bars represent the mean ± SD. Source data are provided as a Source Data file.

of the nanoparticles to an "on" state, concomitant with the liberation of reduced Fe^{2+} ions (Fig. 2M).

The fluorescence "off-on" modulation exhibited by the UCNP-Cro/FA nanoparticles in response to Fe^{3+} ions and NIR irradiation, coupled with the subsequent release of Fe^{2+} ions, underscored their potential for tumor therapy, which motivated us to conduct the next experiment.

Cellular uptake and subcellular localization of UCNP-Cro/FA

MCF-7 breast cancer cells are widely acknowledged for their high expression levels of folate receptors (FRs), as demonstrated in numerous previous studies[33,35]. Consequently, they are considered to be an ideal model for investigating the efficacy and mechanisms of FA-conjugated nanoparticles (UCNP-Cro/FA) synthesized in this study. To explore the uptake efficiency of UCNP-Cro/FA nanoparticles in MCF-7 cells, nanoparticles without the FA ligand (UCNP-Cro) were employed as a control, and the difference in their performance was evaluated by bio-TEM and confocal laser scanning microscopy (CLSM). As shown in Fig. 3A and Supplementary Fig. 15, in the initial 4 h, MCF-7 cells co-incubated with UCNP-Cro/FA exhibited stronger red fluorescence and greater nanoparticle internalization compared to those exposed to UCNP-Cro. The finding indicated that surface modification of nanoparticles with FA could significantly accelerate their entry into MCF-7 cells, possibly as a result of the interaction between FA and FRs overexpressed on the cell surface. To examine whether the UCNP-Cro/FA nanoparticles uptake was indeed mediated via the FRs, we tested internalization efficiency of the nanoparticles in four different tumor cell lines (4T1, MCF-7, HeLa, and A549) with varying levels of FR expression (Supplementary Figs. 16, 17). The result showed that HeLa cells (with higher FR expression) exhibited the highest fluorescence intensity, followed by MCF-7 and 4T1 cells, while A549 cells (with no FR expression) showed minimal fluorescence. Additionally, competitive inhibition experiments results demonstrated that the addition of excess free FA led to a significant reduction in UCNP-Cro/FA uptake in FR-positive cell lines (HeLa, MCF-7, and 4T1), with no significant effect on FR-negative A549 cells. Together, these findings substantiated the mechanism of FR-dependent internalization of UCNP-Cro/FA nanoparticles.

Remarkably, with further extension of the incubation time, the fluorescence intensity of the UCNP-Cro/FA group gradually decreased and essentially disappeared after 8 h, implying an intracellular "on to off" switch of UCNP-Cro/FA. To investigate the underlying reasons for this phenomenon, we further applied CLSM to inspect the subcellular localization of UCNP-Cro/FA nanoparticles within cells. As presented in Fig. 3B, in the UCNP-Cro/FA group, the red fluorescence of nanoparticles mostly overlapped with the green fluorescence of lysosome and showed a yellow color, proving their accurate localization in the lysosome organelle. Conversely, the merged image in the UCNP-Cro group presented two separate colors, implying a random cytoplasmic distribution. Additionally, the colocalization analysis displayed a higher coincidence of two fluorescent pixels (Fig. 3C) and a larger Pearson's correlation coefficient (PCC) in the UCNP-Cro/FA group (Pr = 0.95) compared to UCNP-Cro group (Pr = 0.43), indicating that FA receptor-mediated endocytosis could facilitate the accumulation of nanoparticles in lysosomes. Notably, lysosome, as an iron turnover organelle, contains abundant free Fe^{3+} ions originating from the degradation of iron-containing proteins. Therefore, the UCNP-Cro/FA nanoparticles concentrated in the lysosomes could coordinate with Fe^{3+} ions, which explained the quenching of their intrinsic fluorescence after internalization.

The induction of ferritinophagy

Given that intracellular iron is tightly regulated and transits through lysosomal compartments, we explored the effect of UCNP-Cro/FA nanoparticles on iron homeostasis. The intracellular Fe^{2+} ion level was first assessed using FeRhoNox-1, a probe capable of traversing cell membranes and reacting with Fe^{2+} ions to generate orange fluorescent products. As depicted in Fig. 3D, the lowest intensity of orange fluorescence was observed in cells treated with the UCNP-Cro/FA group compared to the parallel groups. Quantitative analysis further substantiated this observation, revealing a significant reduction in the intracellular Fe^{2+} ion level within the UCNP-Cro/FA-treated cells (Fig. 3E, F). Additionally, we also found that the attenuation of the orange fluorescence signal in the UCNP-Cro/FA group presented a time-dependent mode (Supplementary Fig. 18). These results were consistent with the idea that the coordination of UCNP-Cro/FA nanoparticles with Fe^{3+} ions would block the transport of iron from lysosomes to the cytoplasm. Exactly, the interaction disrupted the typical pathway wherein Fe^{3+} ions underwent reduction to Fe^{2+} ions via a six-transmembrane epithelial antigen of prostate 3 (STEAP3)-mediated reaction followed by transportation to the cytoplasm via divalent metal transporter 1 (DMT1). Consequently, with Fe^{3+} ions being sequestered in the lysosomal compartments due to nanoparticle coordination, there was a resulting deficiency of iron in the cytoplasm.

The cytosolic labile iron pool (LIP) has been assumed to serve a dual role: as a rapidly adjustable source of iron for immediate metabolic utilization and as a target for sensing by iron-regulatory proteins (IRPs), which orchestrate iron uptake and compartmentalization via transferrin receptors and ferritin[36]. Therefore, under the aforementioned conditions of iron depletion, it is reasonable to assume that tumor cells would activate the autophagic degradation of ferritin to replenish the available cellular iron pool. For verification, the formation of LC3 puncta, a commonly used marker of autophagosome formation, was monitored in MCF-7 cells after different treatments via immunofluorescence imaging (Fig. 3H and Supplementary Fig. 19). The observation revealed a substantial increase in the number of LC3 puncta within the UCNP-Cro/FA group. Furthermore, a noteworthy correlation was observed wherein the evolution trend of LC3 fluorescence in all samples exhibited an inverse relationship with intracellular Fe^{2+} ion levels, which confirmed that iron starvation triggered compensatory activation of the autophagic cascade. The hypothesis was consistently supported by the TEM observation on UCNP-Cro/FA-treated cells, in which more autophagic vesicles were present after 12 h of incubation compared to 4 h of incubation (Supplementary Fig. 20).

After confirming UCNP-Cro/FA-induced autophagosome formation, the autophagic degradation of ferritin was determined by western blotting. During a typical ferritinophagy process, ferritin first binds to nuclear receptor coactivator 4 (NCOA4) and undergoes trafficking to autophagosomes, which then fuse with lysosomes to degrade iron-laden ferritin and liberate stored iron. As shown in Fig. 3G, accompanied by negligible changes in the control and UCNP-FA groups, the UCNP-Cro group displayed a slight increase in NCOA4 expression alongside a slight reduction in ferritin heavy chain (FTH) expression, while the expression of NCOA4 was significantly elevated and the expression of FTH was markedly diminished in the UCNP-Cro/FA group. This phenomenon was further confirmed by semi-quantitative analysis (Fig. 3I, J). In conclusion, we demonstrated that UCNP-Cro/FA nanoparticles, with efficient cellular uptake and lysosomal localization, would sequester more Fe^{3+} ions than UCNP-Cro nanoparticles, thereby inducing more pronounced iron deficiency stress and subsequently eliciting enhanced ferritinophagy. Advantageously, an intracellular positive feedback loop for facilitating the loading of endogenous iron in lysosomes was established by UCNP-Cro/FA nanoparticles. As depicted in Fig. 3K, these nanoparticles sequestered iron in lysosomes by coordinating with Fe^{3+} ions, consequently initiating ferritin degradation in response to cytoplasmic iron depletion. As a consequence of the lysosomal degradation of ferritin, the released endogenous iron continually coordinated with the nanoparticles, leading to lysosomal enrichment with iron. This

https://doi.org/10.1038/s41467-025-58124-7

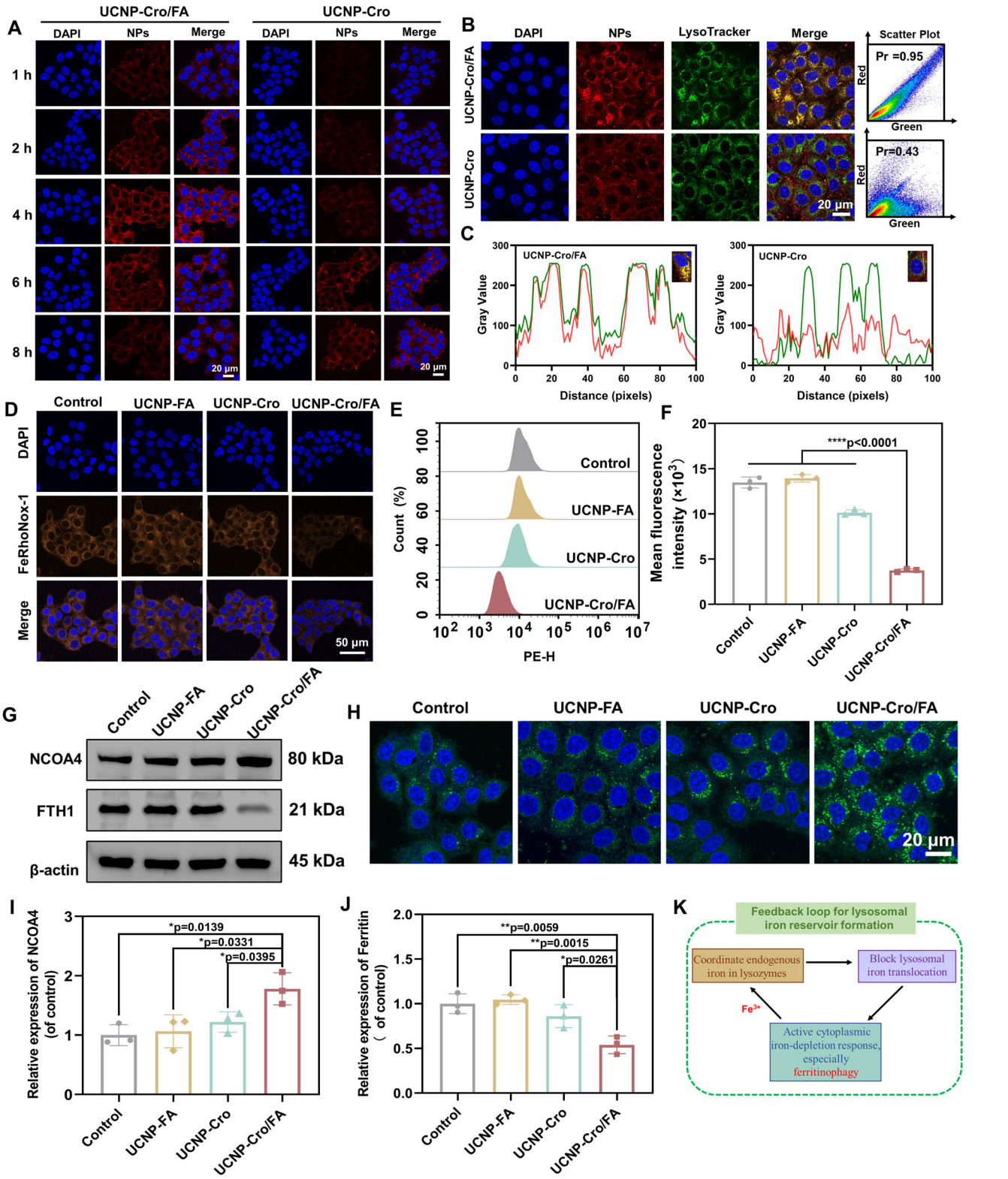

accumulation undeniably presents an opportunity for harnessing endogenous iron to activate the ferroptosis pathway.

In vitro antitumor activity of UCNP-Cro/FA upon irradiation

Next, the cell cytotoxicity of the different formulations was evaluated by CCK-8 assay in the presence or absence of NIR irradiation (Fig. 4A–C). The resulting data indicated that upon NIR irradiation, UCNP-Cro/FA exhibited superior efficacy in suppressing tumor cell proliferation compared with UCNP-Cro and UCNP-FA groups at the same concentration, with corresponding dose-dependent cytotoxicity. In contrast, all three nanoparticles showed negligible toxicity to MCF-7 cells without NIR irradiation, even at concentrations as high as 400 μg/mL. The results were consistently validated by live and dead cell staining using calcein-AM and propidium iodide (PI) dyes, in which the UCNP-Cro/FA + NIR group presented the most intense red fluorescence from dead cells, indicative of the severe treatment-induced

Fig. 3 | Intracellular uptake, subcellular localization and ferritinophagy induction of UCNP-Cro/FA. A Intracellular uptake of the nanoparticles with and without the folate ligand in MCF-7 cells measured by CLSM at prolonged coincubation times. Scale bar=20 μm. **B** Colocalization images of UCNP-Cro/FA or UCNP-Cro with lysosomes in MCF-7 cells after incubation for 4 h. The lysosomes and cell nuclei were stained with Lyso-Tracker Green and DAPI, respectively. Scale bar=20 μm. **C** The plot profile for colocalization analysis of UCNP-Cro/FA or UCNP-Cro with lysosomes. Red line: nanoparticles; Green line: lysosomes. **D** CLSM images (labeled with FeRhoNox−1) of intracellular Fe^{2+} ions after incubation with different formulations. Scale bar=50 μm. E, F) Quantitative analysis of intracellular Fe^{2+} ion levels after incubation with different formulations ($n = 3$ independent experiments in each group). Statistical significance was calculated using an unpaired two-tailed t-test. G) Western blot analysis of the expression levels of ferritinophagy-related proteins (NCOA4 and FTH) after incubation with different formulations. **H** Immunofluorescence images of MCF-7 cells showing the formation of LC3 puncta after incubation with different formulations. Scale bar=20 μm. **I, J** Semi-quantification of NCOA4 and FTH expression based on the western blot results ($n = 3$ independent experiments in each group). Statistical significance was calculated using an unpaired two-tailed t-test. **K** The artificial intracellular positive feedback loop of lysosomal iron reservoir formation. All experiments were repeated three times independently with similar results. Error bars represent the mean ± SD. Source data are provided as a Source Data file.

cellular damage (Fig. 4D). Similarly, the quantitative results of Annexin V-FITC and PI double staining indicated minimal cell death in the control, the UCNP-FA, and the test group without NIR irradiation, while a notable increase in cell death, reaching 79.97%, was observed in the UCNP-Cro/FA + NIR group compared to the UCNP-Cro+NIR group (24.45%) (Supplementary Fig. 21). The variance in cell survival across diverse treatment regimens elucidated the indispensable role of NIR irradiation and Cro molecules in eliciting cellular damage.

In light of the aforementioned findings suggesting the capability of the up-converted UV emitted from UCNPs to trigger the reduction release of iron ions coordinated on the UCNP-Cro/FA nanoparticles, we further conducted flow cytometry to quantify the level of intracellular Fe^{2+} ions after UCNP-Cro/FA + NIR treatment. As expected, NIR irradiation caused a significant increase in Fe^{2+} ion level in MCF-7 cells incubated with UCNP-Cro/FA, even appreciably surpassing that of the control group (Fig. 4F). This observation demonstrated that the obvious cytotoxicity of UCNP-Cro/FA upon NIR irradiation may be attributed to a sudden overload of redox-active iron (Fe^{2+}) ions. To further investigate whether the mechanism of the obtained increase in the intracellular Fe^{2+} ion level was associated with NCOA4-mediated ferritinophagy, tumor cells were pretreated with an autophagy inhibitor (3-methyladenine, 3-MA) before exposure to UCNP-Cro/FA + NIR. Notably, the autophagy inhibitor resulted in a considerable reduction in the intracellular Fe^{2+} ion level, accompanied by a marked improvement in cell viability compared to the treatment without the inhibitor (Fig. 4E, F). The findings validated the contribution of ferritinophagy in UCNP-Cro/FA-induced cell death upon NIR irradiation, achieved through the supplementation of endogenous iron.

Building upon the potent cytotoxicity of UCNP-Cro/FA + NIR in MCF-7 cells, we further evaluated the selectivity of this treatment for cancer cells. The results demonstrated that UCNP-Cro/FA + NIR treatment exhibited FR-dependent cytotoxicity, with FR-positive cells (HeLa, MCF-7, and 4T1) showing a significant reduction in cell viability compared to FR-negative A549 cells. Moverover, when excess free folate was used to compete for FR binding, the cytotoxic effect of UCNP-Cro/FA upon NIR irradiation was notably alleviated in the FR-positive tumor cells. In contrast, no significant change in cell viability was observed in FR-negative A549 cells, regardless of the presence of excess folate (Supplementary Fig. 22). These findings collectively suggested that UCNP-Cro/FA nanoparticles, in conjunction with NIR irradiation, were able to effectively against a range of cancer types with abundant FR expression.

Lysosomal dysfunction via endogenous fenton chemistry induced by UCNP-Cro/FA upon irradiation

Due to the abundant H_2O_2 and low acidic environment in lysosomes[37], the reduced Fe^{2+} ions with high catalytic activity could catalyze the production of •OH via Fenton chemistry. To ascertain, intracellular levels of •OH were assessed using hydroxyphenyl fluorescein (HPF) as a probe, which emitted green fluorescence in the presence of •OH. According to CLSM images (Fig. 4G), negligible green fluorescence was detected in cells following treatment with either single NIR irradiation or UCNP-FA + NIR, indicating that neither NIR light nor up-converted UV directly induced intracellular •OH generation. However, upon NIR irradiation, the UCNP-Cro/FA + NIR samples exhibited significantly enhanced green fluorescence than UCNP-Cro/FA without NIR exposure, suggesting that the NIR-to-UV conversion effectively assisted the reduction of Fe^{3+} to Fe^{2+}, thereby facilitating •OH formation. Additionally, under identical laser conditions, the green fluorescence in UCNP-Cro/FA + NIR was more intense than that in UCNP-Cro+NIR, which was due to the fact that UCNP-Cro/FA, with efficient cellular uptake and lysosomal localization, could coordinate a greater amount of Fe^{3+} ions than UCNP-Cro, resulting in a higher release of Fe^{2+} ions through subsequent reduction processes. Similar trends were also observed for the flow cytometric analysis (Supplementary Fig. 23).

Since the produced lysosomal •OH would diffuse disorderly and attack the lysosomal membranes forcefully from the inside, we then employed acridine orange (AO) as an indicator to investigate the integrity of lysosomes. As shown in Fig. 4J and Supplementary Fig. 24, strong red fluorescence of AO within lysosomes was found in the UCNP-Cro/FA group, with no significant differences compared with the untreated control. In contrast, after NIR irradiation, the red fluorescence was significantly attenuated for cells incubated with UCNP-Cro/FA, while the controls (NIR, UCNP-FA + NIR, UCNP-Cro+NIR) still retained the red fluorescence from AO. This finding indicated that upon NIR irradiation, the lysosome-targeted UCNP-Cro/FA induced lysosomal membrane permeabilization (LMP) through endogenous iron-activated Fenton reaction. In addition, to reconfirm oxidative damage-induced LMP, we carried out subcellular fractionation of treated cells to directly measure the localization of cathepsin B (CTSB), a typical intralysosomal enzyme. Western blotting results showed that UCNP-Cro/FA + NIR treatment caused CTSB protein expression decrease in lysosome fraction and its concomitant increase in the cytoplasmic fraction, indicating the spillage of CTSB from damaged lysosomes into the cytosol (Fig. 4H).

The above results suggested a cascade reaction where endogenous Fe^{3+} ions derived from iron-containing proteins could bind with UCNP-Cro/FA nanoparticles and be reduced to Fe^{2+} under NIR irradiation, leading to their dissociation from the nanoparticles. The bolstering of highly reactive Fe^{2+} ions promoted the Fenton reaction within the lysosomal compartment and subsequently evoked LMP (Fig. 4I).

Ferroptosis and pyroptosis evoked by UCNP-Cro/FA upon irradiation

Once triggering LMP, these surplus Fe^{2+} ions could theoretically leak into the cytoplasm, thus inducing lipid oxidation of biological membranes and potentially triggering ferroptosis[22]. To further test whether LMP triggered by UCNP-Cro/FA under NIR condition contributed to the occurrence of ferroptosis, additional studies were performed to explore ferroptosis-related features. First, the morphology of mitochondria was observed using bio-TEM. As depicted in Fig. 5B, cells treated with UCNP-Cro/FA + NIR exhibited distinct mitochondrial morphologic characteristics of ferroptosis, including the absence of mitochondrial cristae and a reduction in mitochondrial size, in contrast to the physiological morphology observed in the control and

https://doi.org/10.1038/s41467-025-58124-7

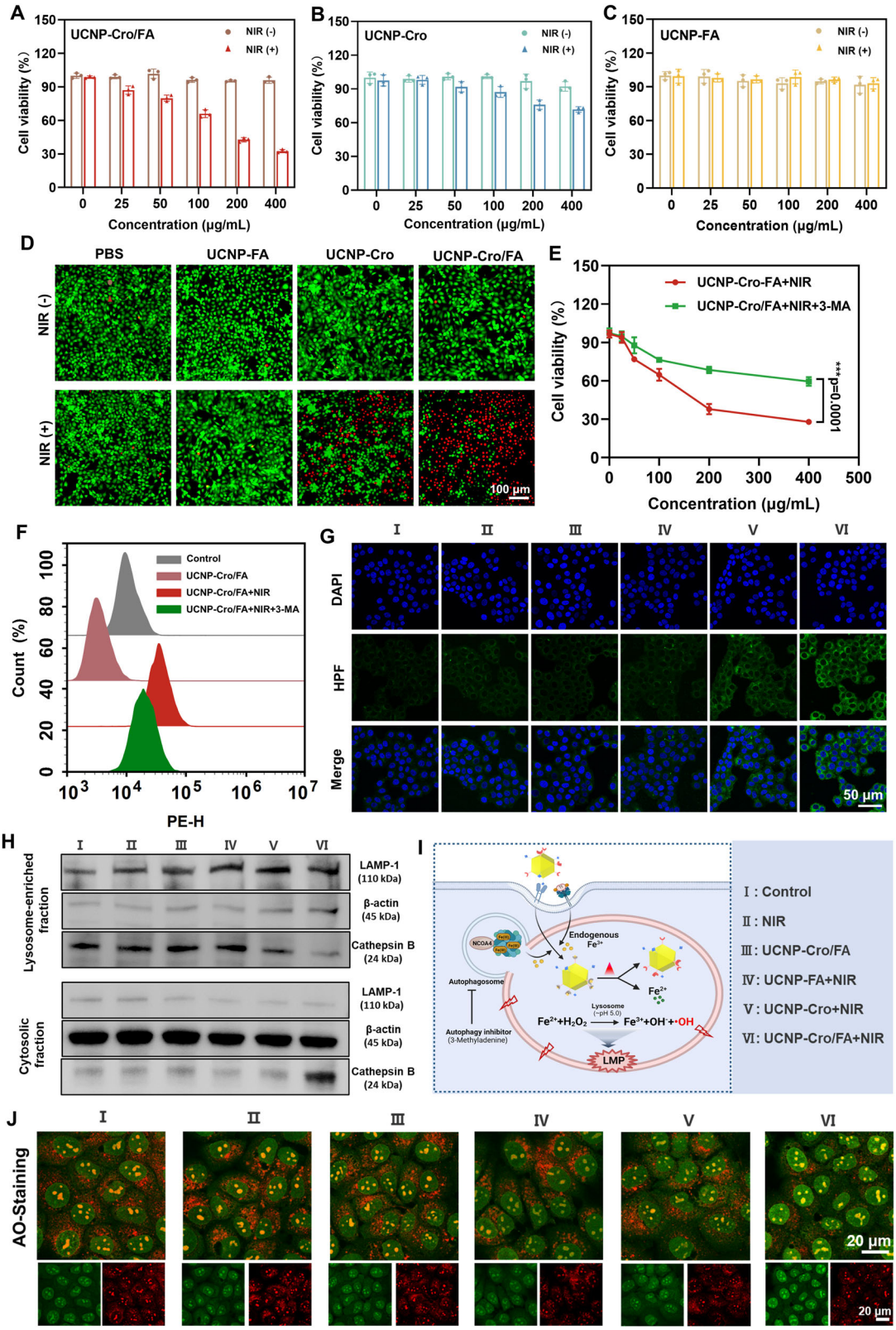

UCNP-Cro/FA groups. In addition to the observed morphological change, various ferroptosis inhibitors, such as ferrostatin-1 (Fer-1), deferoxamine (DFO), and vitamin E (VE), were demonstrated to effectively alleviate the cytotoxicity of UCNP-Cro/FA upon NIR irradiation at the cellular level, hinting the potential of UCNP-Cro/FA as an inducer of ferroptosis upon NIR irradiation (Fig. 5C). Since ferroptosis is typically manifested by the inactivation of glutathione peroxidase 4 (GPX4), the consumption of glutathione (GSH) and the subsequent overwhelming accumulation of lipid peroxides (LPO), we further quantified intracellular GPX4 activity, GSH and LPO levels. Western blot analysis revealed the substantial downregulation of GPX4 in UCNP-Cro/FA + NIR irradiation-treated cells, whereas the other five treatments (control, NIR alone, UCNP-Cro/FA, UCNP-FA + NIR, and UCNP-Cro +NIR) did not achieve identical effects (Fig. 5E).

Fig. 4 | The cytotoxicity, •OH generation and lysosomal membrane permeability induction of UCNP-Cro/FA upon NIR irradiation. A, **B**, **C** Cytotoxicity assay of MCF-7 cells in response to different formulations after 24 h of incubation with or without NIR irradiation (1 W/cm^2, 10 min). $n = 3$ independent experiments in each group. **D** Live/dead staining assay (green: live cells; red: dead cells) of MCF-7 cells after different treatments. Scale bar=100 μm. **E** Relative viability of MCF-7 cells treated by UCNP-Cro/FA + NIR with/without the autophagy inhibitor (3-MA) ($n = 3$ independent experiments in each group). Statistical significance was calculated using an unpaired two-tailed t-test. **F** FC analysis of intracellular Fe^{2+} ion level in MCF-7 cells by FeRhoNox−1 after different treatments. **G** CLSM images of intracellular •OH generation after different treatments. Scale bar=50 μm. **H** Western blot analysis for the evaluation of CTSB in the different subcellular fractions after different treatments. β-actin and LAMP1 were used as cytosolic and lysosomal markers, respectively. **I** Schematic illustration of NIR-controlled UCNP-Cro/FA to induce endogenous ion-mediated LMP. The UCNP-Cro/FA nanoparticles coordinated with endogenous Fe^{3+} ions to sequester them within lysosomes. Upon NIR irradiation, the enhanced Fenton reaction due to the reduction of Fe^{3+} to Fe^{2+} resulting from catalytic UV emitted by UCNP, led to the generation of •OH and subsequent LMP. Created in BioRender. Luwen, Z. (2025) BioRender.com/n85y153. J) CLSM images of AO-stained MCF-7 cells after different treatments for LMP evaluation. Scale bar=20 μm. Experiments in (**D**), (**F**), (**G**), (**H**), and (**J**) were repeated three times independently with similar results. Error bars represent the mean ± SD. Source data are provided as a Source Data file.

Simultaneously, compared with the control group in which the GSH level was defined as 100%, the percentage of intracellular GSH was depleted to 25.4% and 73.8% in the UCNP-Cro/FA + NIR and UCNP-Cro +NIR samples, respectively, with negligible GSH reduction observed in the NIR alone and UCNP-FA + NIR samples (Fig. 5D). These findings, combined with earlier examinations of intracellular ·OH generation in the corresponding treated samples, indicated that NIR-converted Fe^{2+} ions effectively compromised cellular antioxidant defense by facilitating the cell-intrinsic Fenton mechanism. It is known that the deterioration of cellular lipid peroxidation reduction ability induced by GSH/GPX4 depletion is favorable for LPO accumulation. For verification, we employed C11-BODIPY581/591 as a LPO fluorescent sensor, which shifted its maximum emission peak from 590 nm (red) to 510 nm (green) upon oxidation. Although CLSM images showed a decay of red fluorescence and an increase of green fluorescence in the UCNP-Cro+NIR group, demonstrating the production of LPO, the degree of peroxidation was stronger in the UCNP-Cro/FA + NIR group (Fig. 5G, H). The result validated that UCNP-Cro/FA nanoparticles enriched in lysosomes via the FR-mediated endocytic pathway hijacked more lysosomal iron into the cytoplasm upon NIR irradiation via the aforementioned cascade reaction than unmodified FA nanoparticles (UCNP-Cro), thus further promoting LPO production and sensitizing tumor cells to ferroptosis. Besides, malondialdehyde (MDA), the final product of LPOs, is considered another landmark product of ferroptosis. Figure 5I showed that the MDA content in the cells treated with UCNP-Cro/FA + NIR significantly increased 5.14-fold as compared to the control group, providing additional evidence for the occurrence of ferroptosis.

Pyroptosis is a novel form of regulated cell death (RCD) that is driven by the activation of inflammasomes such as nucleotide-binding oligomerization domain (NOD)-like receptor (NLR) family[6]. Specifically, these inflammasomes are stimulated during cell injury and then activate caspase-induced gasdermin (GSDM) cleavage. The resulting N-terminal fragments of GSDM assemble to drill pores on the cell membrane followed by cell swelling with large bubbles and the release of inflammatory cytokines, including interleukin-1β (IL-1β) and lactate dehydrogenase (LDH)[38,39]. It has been reported that LMP with subsequent cathepsins release, particularly CTSB, is a potent activator of the NLRP3 inflammasome and implicated in triggering pyroptosis[40]. In addition to CTSB release, the production of ROS is another common stimulator for inflammasome activation, and previous studies have shown that iron-mediated amplification in ROS levels could induce pyroptosis[8,41]. Encouraged by the successful establishment of iron overload and the translocation of CTSB from lysosomes to the cytosol in MCF-7 cells treated with UCNP-Cro/FA + NIR, we further explored whether this process could induce typical pyroptosis. Microscopic observations demonstrated that dying tumor cells in the UCNP-Cro/FA + NIR group exhibited evident swelling and characteristic membrane blebbing, presenting a pyroptosis-like morphology (Fig. 5J). Subsequently, the levels of LDH and IL-1β in the cell supernatants after different treatments were examined. As shown in Fig. 5K, L, UCNP-Cro/FA + NIR treatment dramatically stimulated LDH and IL-1β release from MCF-7 cells, and the levels increased in culture medium up to 25.8-fold and 6.4-fold, respectively, compared to those in the control group. More importantly, the contents of the two inflammatory molecules in the UCNP-Cro/FA + NIR group significantly surpassed those in the UCNP-Cro+NIR group, meaning that FA-modified UCNP-Cro/FA had a memorably enhanced ability to induce pyroptotic cell death upon NIR irradiation due to a greater degree of lysosome-targeted oxidative stress. Furthermore, western blot analysis revealed UCNP-Cro/FA + NIR treatment significantly upregulated the expression of NLRP3 (Supplementary Fig. 25), indicating activation of the NLRP3 inflammasome. Cleaved-caspase-1 and N-GSDMD, which function downstream of the classical pyroptotic pathway, were also greatly upregulated in the UCNP-Cro/FA + NIR group (Fig. 5M). Notably, the upregulation of NLRP3 and Cleaved-caspase-1 were effectively inhibited by the NLRP3 inhibitor MCC950 (Supplementary Fig. 26), further confirming the involvement of a NLRP3/Caspase-1/GSDMD-dependent pyroptosis pathway in cell death induced by UCNP-Cro/FA + NIR. Meanwhile, GSDMD-mediated membrane pore, one of the hallmarks of pyroptosis, could be observed on the surface of UCNP-Cro/FA + NIR-treated cells under scanning electron microscopy, whereas those in the control and UCNP-Cro/FA groups remained intact (Fig. 5F). Next, we knocked down GSDMD in MCF-7 cells using siRNA (Supplementary Fig. 27) and then assessed the cytotoxicity of UCNP-Cro/FA + NIR on GSDMD-deficient cells. As shown in Supplementary Fig. 28, silencing GSDMD significantly enhanced cell survival, providing additional evidence for the occurrence of pyroptosis.

Taken together, these data confirmed that when exposed to NIR, UCNP-Cro/FA was able to harm the lysosomal membrane by cytotoxic •OH generated from an enhanced lysosomal Fenton reaction, which subsequently induced the outflow of lysosomal contents (e.g., iron and cathepsin B) that in turn initiated ferroptosis and caspase-1 activation-mediated pyroptosis (Fig. 5A).

As a proof-of-concept, we further investigated whether pyroptosis and ferroptosis initiated by UCNP-Cro/FA upon NIR irradiation is universal. The bright-field images shown in Supplementary Fig. 29A indicated that 4T1 and Hela cells in UCNP-Cro/FA group exhibited distinct morphological features of pyroptosis (bubble-like protrusions), which were comparatively unremarkable in A549 cells lacking FR expression. In addition, the application of the pyroptosis inhibitor VX765 and the ferroptosis inhibitor Fer-1 significantly restored cell viability in these tumor cells subjected to UCNP-Cro/FA + NIR treatment (Supplementary Fig. 29B). Collectively, these results demonstrated the broad-spectrum efficacy of UCNP-Cro/FA in inducing both pyroptosis and ferroptosis upon NIR irradiation, a process that was potentiated through FR-mediated endocytosis and subsequent lysosomal iron hijacking.

In vivo performance of UCNP-Cro/FA

To identify the optimal therapeutic window in vivo, we conducted biodistribution studies of different nanoformulations in MCF-7-tumor-bearing mice by fluorescence imaging. According to the in vivo imaging results (Fig. 6A), the Cro fluorescence in the UCNP-Cro and UCNP-

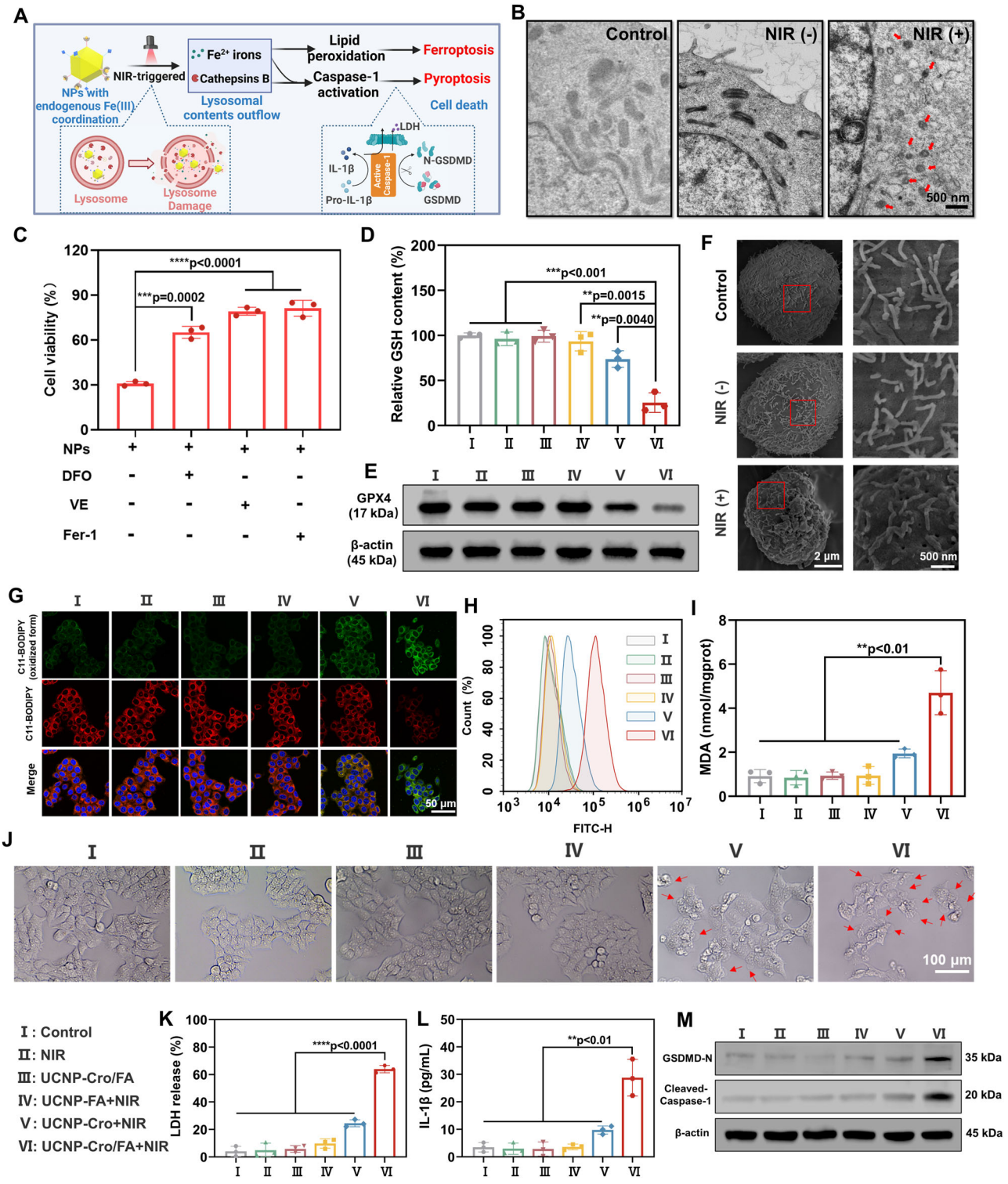

Cro/FA groups continuously increased in tumor regions within 12 h after systemic administration. Notably, compared to the UCNP-Cro group, the UCNP-Cro/FA group showed a significantly stronger fluorescence signal in tumors at 12 h post-injection, confirming the active targeting capability of the FA-modified formulation in vivo. Interestingly, at a later time point (24 h post-injection), even though the tumor fluorescence intensity in the UCNP-Cro group remained almost unchanged, it nearly vanished in the UCNP-Cro/FA group. Based on the above results of cellular uptake study, this phenomenon could be explained by the fluorescence quenching of UCNP-Cro/FA due to its coordination with endogenous Fe^{3+} ions in the lysosomes. To ascertain this, we replaced Cro molecules with indocyanine green (ICG), a comparable NIR fluorescent dye but lacking iron-chelating properties, and then traced the UCNP-ICG/FA in vivo after intravenous injection. As depicted in Fig. 6A, 24 h later, the tumor-specific fluorescence signal remained robust, suggesting nanoparticle retention. This finding further supported that the decrease in fluorescence observed in the UCNP-Cro/FA group was attributable to the "switching off" of UCNP-Cro/FA fluorescence rather than the removal of nanoparticles in vivo.

The major organs and tumors of mice were harvested at 24 h post-injection for thorough fluorescence analysis (Fig. 6B, C). As expected, the fluorescence intensities of all three nanoformulations in tumors

Fig. 5 | Representative characterization of ferroptosis and pyroptosis evoked by UCNP-Cro/FA upon irradiation. A The process of UCNP-Cro/FA nanoparticles initiating irreversible tumor cell death via ferroptosis and pyroptosis upon NIR irradiation. Created in BioRender. Luwen, Z. (2025) BioRender.com/n87w615. B) TEM observations of mitochondrial morphological changes in MCF-7 cells treated by UCNP-Cro/FA with or without NIR irradiation. Scale bar=500 nm. **C** Relative viability of MCF-7 cells treated with UCNP-Cro/FA + NIR in the presence of different ferroptosis inhibitors ($n = 3$ independent experiments in each group). Statistical significance was calculated using an unpaired two-tailed t-test. **D** Relative GSH content of MCF-7 cells after different treatments ($n = 3$ independent experiments in each group). Statistical significance was calculated using an unpaired two-tailed t-test. **E** Western blot analysis of GPX4 expression in MCF-7 cells after different treatments. **F** Bio-SEM images of MCF-7 cells and corresponding higher-magnification images of the red-framed area after treatment with UCNP-Cro/FA with or without NIR irradiation. Scale bar=2 μm, and scale bar=500 nm in enlarged images. **G**, **H** CLSM observation and FCM quantitative analysis of MCF-7 cells stained with C11-BODIPY after different treatments to detect lipid peroxidation levels. Scale bar=50 μm. I) MDA content of MCF-7 cells after different treatments ($n = 3$ independent experiments in each group). Statistical significance was calculated using an unpaired two-tailed t-test. **J** The optical microscopy images of MCF-7 cells after different treatments. The red arrows point toward bubble-like protrusions on the surface of cell membrane. Scale bar=100 μm. **K**, **L** Release of LDH (**K**) and IL-1β (**L**) from MCF-7 cells after different treatments ($n = 3$ independent experiments in each group). Statistical significance was calculated using an unpaired two-tailed t-test. **M** Western blot of the expression levels of pyroptosis-related proteins (GSDME-N and cleaved-caspase-1) in MCF-7 cells after different treatments. Experiments in (**B**), (**F**), (**E**), (**G**), (**J**) and (**M**) were repeated three times independently with similar results. Error bars represent the mean ± SD. Source data are provided as a Source Data file.

were higher than those observed in the heart, liver, spleen, lung and kidney. Moreover, the fluorescence emitted by UCNP-ICG/FA in tumor tissues was pronounced, whereas that of UCNP-Cro/FA was relatively weak, which was consistent with the in vivo results. To accurately assess UCNP accumulation, we conducted additional ICP-OES analysis to quantify the yttrium (Y) content in the excised tumors (Supplementary Fig. 30). The data showed that the higher Y content was distributed in the tumors of mice injected with the FR-modified nanoformulation than those of non-modified one, which not only demonstrated the superior tumor targeting and retention properties of UCNP-Cro/FA, but also proved again that most of the nanoparticles reaching the tumor site 24 h after injection were taken up by tumor cells and coordinated with endogenous Fe^{3+} ions in lysosomes, as evidenced by their fluorescence quenching. Importantly, these collective results provided a reference for determining the optimal time point for NIR irradiation treatment in the tumor area.

After injections of different nanoformulations every other day for a total of three times, mice in all groups were sacrificed, and their tumors were collected for subsequent analysis of the Fe^{2+} ion contents and ferritin levels (Fig. 6D). Unsurprisingly, compared with the parallel treatment groups, the lowest Fe^{2+} content as well as the greatest reduction in ferritin were observed in the UCNP-Cro/FA group, while those in the UCNP-ICG/FA group was not significantly different from the control group (Fig. 6E–G). The results indicated that UCNP-Cro/FA was capable of destroying iron homeostasis of MCF-7 tumor cells in vivo, leading to cytoplasmic iron depletion and ferritin degradation. And it is reasoned that this effect was specifically attributed to Cro molecules, which impeded the transport of iron ions from the lysosome to the cytoplasm.

In vivo antitumor activity of UCNP-Cro/FA upon irradiation

Building on the effective induction of ferroptosis and pyroptosis by UCNP-Cro/FA + NIR in vitro, we investigated whether a similar inhibitory effect could occur in an MCF-7 tumor-bearing nude mouse model. The mice were randomly allocated into six groups for different treatments: (1) Control, (2) NIR, (3) UCNP-Cro/FA, (4) UCNP-FA + NIR, (5) UCNP-Cro+NIR, and (6) UCNP-Cro/FA + NIR. NIR irradiation (980 nm, 2 W/cm^2, 10 min) was performed in the tumor regions of the appropriate groups 24 h after intravenous injection according to the in vivo fluorescence imaging results (Fig. 7A). The tumor volume of the mice in each group was measured every two days for three weeks. Figure 7B illustrated that the tumors in the control, NIR, UCNP-Cro/FA, and UCNP-FA + NIR groups exhibited a rapid growth trend, suggesting a negligible antitumor effect. In contrast, UCNP-Cro/FA + NIR significantly inhibited tumor growth, whereas the UCNP-Cro+NIR group showed suboptimal inhibition due to inadequate targeting. At the end of the 21-day treatment period, tumors were extracted for direct comparison, and the tumor weights and images in corresponding groups were consistent with the trends of tumor growth curves, clarifying the superior antitumor efficacy of UCNP-Cro/FA upon NIR irradiation compared to the other treatments (Fig. 7C, D). Ulteriorly, the tumor tissue samples were analyzed via terminal deoxynucleotidyl transferase-mediated dUTP nick-end labeling (TUNEL) and hematoxylin and eosin (H&E) staining, where the UCNP-Cro/FA + NIR group presented the most pronounced cytomorphological changes, including nucleus contraction and cytoplasmic leakage, along with the highest level of cell death characterized by bright green fluorescence in the cell nucleus (Fig. 7J). Moreover, analysis of the survival curves revealed that the median survival time of the mice treated with UCNP-Cro/FA + NIR was 16 days longer than that of the control group, demonstrating excellent therapeutic potential (Fig. 7E). To verify the antitumor mechanism of UCNP-Cro/FA + NIR, immunohistochemical staining was conducted on the extracted tumor tissues (Fig. 7J). Corresponding to the results of the in vitro analysis, the elevated cleaved-caspase 1 expression caused by UCNP-Cro/FA + NIR treatment revealed the occurrence of pyroptosis during cancer cell death (Fig. 7G). Additionally, the prominent downregulation of GPX4 expression and increased MDA content in the UCNP-Cro/FA + NIR group confirmed the involvement of ferroptosis in its anticancer effects (Fig. 7H, I). These results demonstrated that this ferroptosis and pyroptosis awakened strategy, which hijacked endogenous iron to boost Fenton reaction-mediated LMP, could exert potent tumor inhibition effect.

In addition to the above therapeutic evaluation, we also studied the safety of the nanoformulations in MCF-7 tumor-bearing mice. Stable body weight curves and no obvious histological abnormalities in H&E-stained images of major organs were observed in all treated groups, suggesting the good biocompatibility of these nanoparticles (Fig. 7F and Supplementary Fig. 31). Meanwhile, the blood biochemical analysis showed that liver function-related indicators, including alanine aminotransferase (ALT) and aspartate transaminase (AST), and kidney function-related indicators, including urea nitrogen (BUN) and creatinine (CR), were within the normal ranges, indicating that the unique spatiotemporal activatable property of UCNP-Cro/FA in tumors effectively protected the mice from other organ damage (Supplementary Fig. 32).

Taken together, these results showed that upon NIR irradiation, the UCNP-Cro/FA nanoplatform exhibited exceptional in vivo antitumor efficacy through a combination of ferroptosis and pyroptosis, with no adverse effects on normal tissues.

In vitro and in vivo immune stimulation effects of UCNP-Cro/FA upon irradiation

Previous studies have shown that both pyroptosis and ferroptosis may lead to immunogenic cell death (ICD)[42,43], so there is an opportunity to use this combination with immunotherapy for synergistic effects. To explore this effect, we first studied the damage associated molecular patterns (DAMPs) released from UCNP-Cro/FA + NIR-treated 4T1 cells, including calreticulin (CRT), adenosine triphosphate (ATP) and high

https://doi.org/10.1038/s41467-025-58124-7

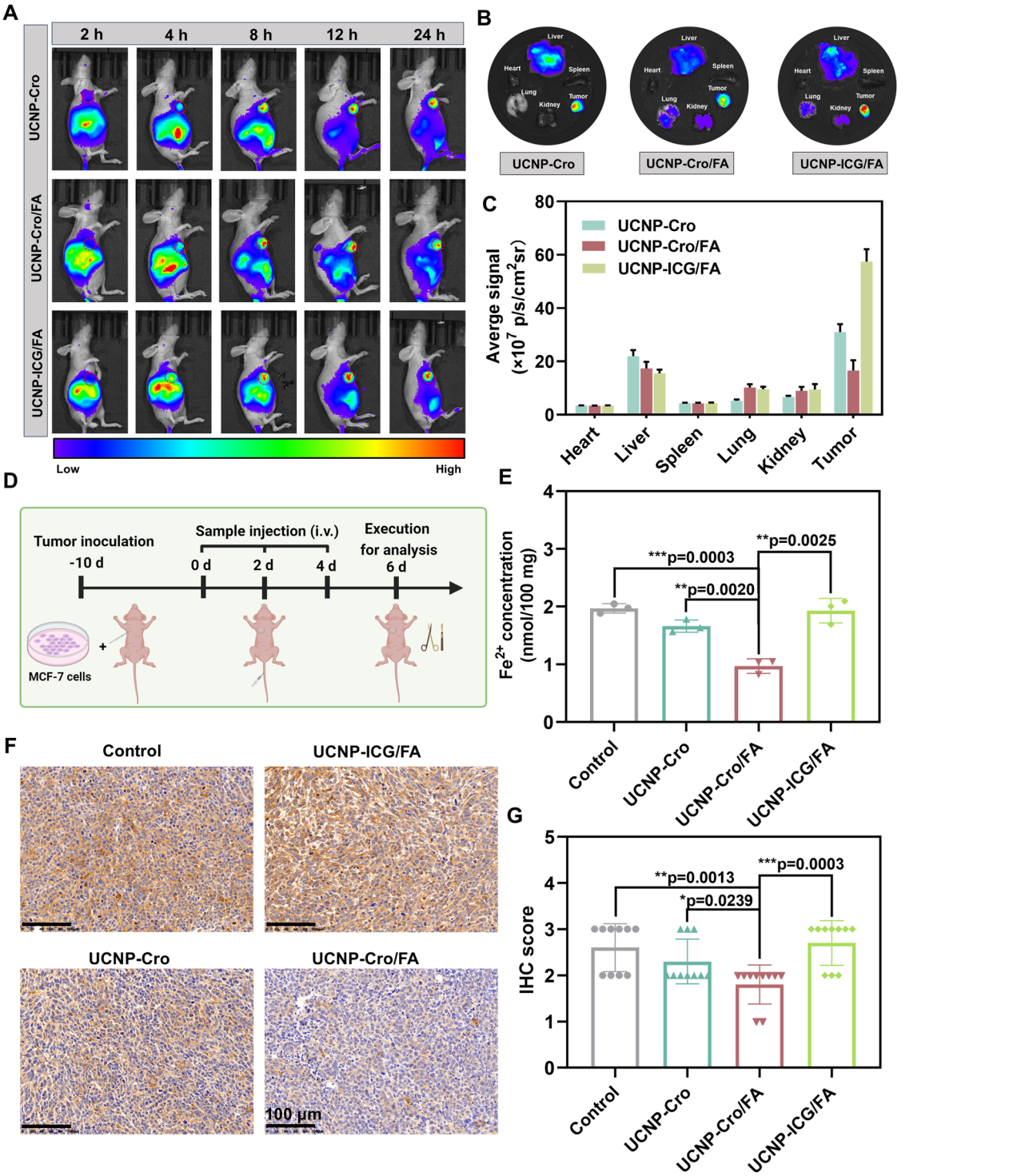

Fig. 6 | Biodistribution and Ferritinophagy induction of UCNP-Cro/FA. A In vivo fluorescence imaging of MCF-7 tumor-bearing mice at different time points after intravenous injection of UCNP-Cro, UCNP-Cro/FA and UCNP-ICG/FA nanoparticles. **B**, **C** Ex vivo fluorescence imaging (**B**) and semiquantitative analysis (**C**) of major organs and tumors harvested at 24 h post-injection of UCNP-Cro, UCNP-Cro/FA and UCNP-ICG/FA nanoparticles ($n = 3$ mice in each group). **D** Scheme of experimental plan to evaluate Fe^{2+} ion contents and ferritin levels in tumor tissues after the indicated treatments. Created in BioRender. Luwen, Z. (2025) BioRender.com/n87w615. **E** Fe^{2+} ion contents in tumor tissues after intravenous injection of different nanoformulations ($n = 3$ mice in each group). Statistical significance was calculated using an unpaired two-tailed t-test. **F** Representative ferritin immunohistochemical staining images of tumor tissues after intravenous injection of different nanoformulations. Scale bar=100 μm. **G** The IHC scores of ferritin in tumor tissues after intravenous injection of different nanoformulations. $n = 10$ images examined over three independent experiments. Statistical significance was calculated using an unpaired two-tailed t-test. Experiments in (**A**), (**B**) and (**F**) were repeated three times independently with similar results. Error bars represent the mean ± SD. Source data are provided as a Source Data file.

https://doi.org/10.1038/s41467-025-58124-7

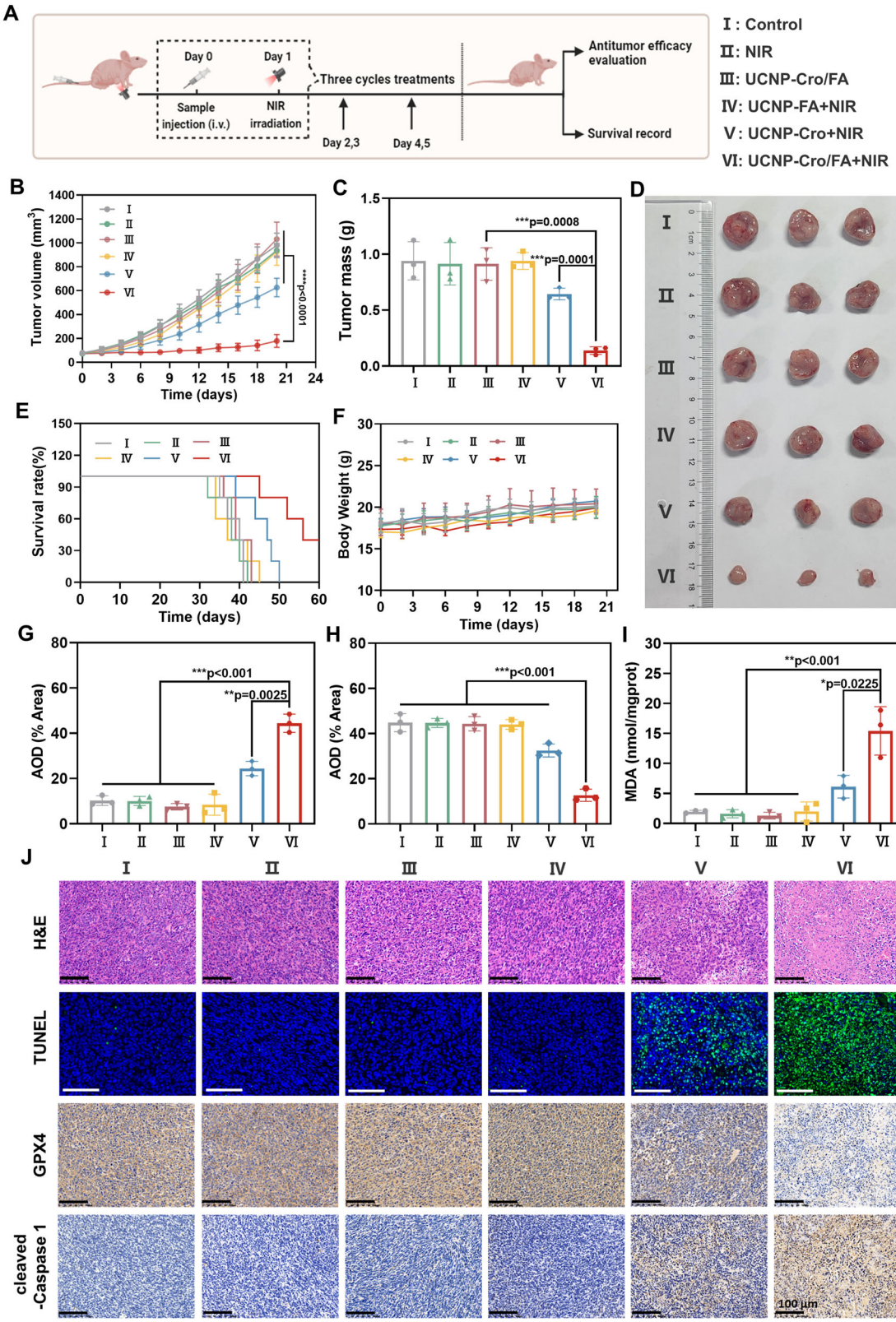

mobility group box 1 (HMGB1), which are important features of ICD. The results of the immunofluorescence (Fig. 8A, B) and ELISA (Fig. 8C, D) assays indicated that UCNP-Cro/FA + NIR treatment significantly upregulated the exposure of CRT, and promoted the secretion of HMGB1 and ATP from cells. Given that these components collaboratively act as a "find and eat me" signal for antigen-presenting cells (APCs)[44], we then evaluated the ability of 4T1 cells pretreated with UCNP-Cro/FA + NIR to induce dendritic cells (DCs) maturation in vitro using Transwell assays. As displayed in Fig. 8E, F and Supplementary Fig. 33, the copositivity of CD86 and CD80 dramatically increased from 17.85 ± 1.02% (control) to 43.14 ± 2.78% in the UCNP-Cro/FA + NIR group, manifesting effective activation of DCs triggered by pyroptosis and ferroptosis cells. The DC media were also collected to measure the secreted immune cytokines by mature DCs, which contribute to

Fig. 7 | In vivo therapeutic efficacy of UCNP-Cro/FA upon irradiation. A The schedule of cancer treatment in vivo. Each group received an intravenous injection of various formulations followed by NIR irradiation (980 nm, 2 W/cm^2, 10 min) in those light-involved groups. Created in BioRender. Luwen, Z. (2025) BioRender.com/n87w615. **B** The tumor growth curves of mice under different treatments ($n = 8$ mice in each group). Statistical significance was calculated using an unpaired two-tailed t-test. **C** Tumor weights of mice at the end of different treatments ($n = 3$ mice in each group). Statistical significance was calculated using an unpaired two-tailed t-test. **D** Photos of excised tumors at the end of different treatments. **E** Survival rates of mice under different treatments ($n = 5$ mice in each group). F) Body weight curves of mice during the therapeutic period ($n = 8$ mice in each group). **G** Quantitative analysis of immunohistochemical staining for cleaved-caspase 1 ($n = 3$ mice in each group). Statistical significance was calculated using an unpaired two-tailed t-test. **H** Quantitative analysis of immunohistochemical staining for GPX4 ($n = 3$ mice in each group). Statistical significance was calculated using an unpaired two-tailed t-test. **I** MDA content in the tumor tissues after different treatments ($n = 3$ mice in each group). Statistical significance was calculated using an unpaired two-tailed t-test. J) Representative images of tumor slices from different groups for H&E staining, TUNEL staining, and immunohistochemical staining of GPX4 and cleaved-caspase 1. Scale bar=100 μm. Experiments were repeated three times independently with similar results. I: Control, II: NIR, III: UCNP-Cro/FA, IV: UCNP-FA + NIR, V: UCNP-Cro+NIR, VI: UCNP-Cro/FA + NIR. Error bars represent the mean ± SD. Source data are provided as a Source Data file.

following activation and proliferation of T lymphocytes. As expected, the levels of both tumor necrosis factor-α (TNF-α) and interleukin-6 (IL-6) were found to be the highest in the UCNP-Cro/FA + NIR group (Fig. 8G, H). These results confirmed that under NIR irradiation, UCNP-Cro/FA could efficiently enhance tumor immunogenicity by inducing pyroptosis and ferroptosis, then boost DC maturation and antigen presentation for initiating antitumor immune responses.

It is noteworthy that FA binds equally well to both major isoforms of the FR-that is, FR-α, which is primarily expressed on malignant cells, and FR-β, which is upregulated on M2 tumor-associated macrophages (TAMs)[45,46]. Considering that TAMs tend to polarize into the immune escape-related M2 phenotype within the tumor microenvironment, it is possible that UCNP-Cro/FA nanoparticles are moderately internalized by M2-type macrophages after on-demand accumulation in tumor tissue. Since macrophages are highly plastic and can be modulated by various stimuli, including iron[47], and UCNP-Cro/FA has been demonstrated to mobilize cellular endogenous iron upon NIR irradiation (as shown in Fig. 4F), we sought to further investigate the impact of UCNP-Cro/FA + NIR on macrophage polarization. During the study, RAW 264.7 cells were first induced to form M2 type by interleukin-4 (IL-4) stimulation, and then the expression of CD86 (M1 marker) and CD206 (M2 marker) in these cells after different treatments was analyzed by FCM. As shown in Supplementary Fig. 34, the UCNP-Cro/FA + NIR group exhibited the lowest proportion (22.89%) of M2 phenotype and the highest proportion (75.15%) of M1 phenotype compared to the model and other treatment groups. Moreover, the mRNA levels of M1 polarization-related gene, including iNOS, TNF-α, and IL-1β, were significantly upregulated, whereas the M2 polarization-related genes, including Arg-1, IL-10, and TGF-β, were downregulated after treatment with UCNP-Cro/FA + NIR (Supplementary Fig. 35 and Supplementary Table 2). These results proved that UCNP-Cro/FA effectively promoted M2-to-M1 repolarization of macrophages upon NIR irradiation, underscoring its considerable potential in activating immune responses and reversing the immunosuppressive TME.

Encouraged by the effective immune activation of UCNP-Cro/FA + NIR achieved via a two-pronged in vitro approach (triggering pyroptosis and ferroptosis-mediated ICD, and regulating the M1 polarization of TAMs), we established a 4T1 tumor-bearing mouse model to further investigate its potential immune properties in vivo. Here, the experimental groupings in vivo were optimized into three groups: control, UCNP-Cro/FA and UCNP-Cro/FA + NIR groups, based on the findings from the in vitro immune activation assays, and the construction method and treatment regimen are shown in Supplementary Fig. 36.

Similar to the treatment effect observed in the MCF-7 tumor model, UCNP-Cro/FA + NIR effectively inhibited 4T1 tumor growth, with no significant weight loss throughout the treatment (Supplementary Figs. 37, 38). At the end of the treatment, we first evaluated the polarization of the TAMs in tumor tissues. Flow cytometry analysis (Fig. 9A, B and Supplementary Fig. 39) showed that the polarization of TAMs towards the M1-type was pronounced in the UCNP-Cro/FA + NIR group, as shown by a decrease in the proportion of M2-type TAMs from 27.93 ± 2.23% to 8.16 ± 1.36% and an increase in the proportion of M1-type TAMs from 4.53 ± 1.07% to 22.28 ± 2.37%, using the control group as a comparison, which proved the improvement of the immune microenvironment. From the experiments assessing DCs maturation in Fig. 9C, D, Supplementary Fig. 40, it can be seen that the highest maturity of DCs in the lymph nodes appeared in the UCNP-Cro/FA + NIR group, which was mainly attributed to the exposure to massive amounts of TAAs and DAMPs. As APCs, mature DCs are important for the presentation of antigens to T cells for adaptive antitumor immunity, so the activation of helper T cells ($CD4^+$ T cells) and cytotoxic T lymphocytes ($CD8^+$ T cells) in the spleens of mice was further analyzed. As anticipated, following treatment with UCNP-Cro/FA + NIR, there was a significant increase in both $CD4^+$ and $CD8^+$ T cells, revealing a strong activation of the immune response (Fig. 9E–G and Supplementary Fig. 41). Next, we quantitatively evaluated the infiltration of $CD4^+$ and $CD8^+$ T cells into the tumor tissues of the different treatment groups. As shown in Fig. 9H–J and Supplementary Fig. 42, compared with those in the control group, the amount of $CD4^+$ and $CD8^+$ T-cell infiltration increased ≈3.9-fold and ≈4.3-fold, respectively, in tumors treated with UCNP-Cro/FA + NIR. In addition, the enhanced secretion of pro-inflammatory cytokines, including IL-6, TNF-α, and interferon-γ (IFN-γ), at the tumor site further indicated that UCNP-Cro/FA + NIR treatment could induce a potent antitumor immune response in mice (Supplementary Fig. 43). In summary, UCNP-Cro/FA combined with NIR treatment effectively induced the polarization of TAMs toward the M1 phenotype, promoted DC maturation, and facilitated T cell recruitment. These actions collectively contribute to the reprogramming of the immunosuppressive TME, thereby triggering a robust anti-tumor immune response in vivo (Fig. 9K).

Discussion

In conclusion, we designed an up-conversion nanoparticle functionalized with folic acid and croconaine molecules (UCNP-Cro/FA). It could be specifically internalized by tumor cells via folate receptor-mediated endocytosis and precisely localize to lysosomes, in which Cro molecules coordinated with endogenous Fe^{3+} ions to inhibit their translocation. Mechanism studies showed that this special strategy could activate cytoplasmic iron deficiency stress, notably augmenting ferritinophagy to mobilize the stored endogenous iron, which established an artificial intracellular positive feedback loop conducive to the formation of lysosomal iron reservoirs. Upon NIR light activation, the UV-emitting upconversion core enabled the reduction of Fe^{3+} to Fe^{2+}, initiating LMP through Fenton reaction-based ·OH generation. In vitro pharmacodynamic studies demonstrated that this process further triggered irreversible tumor cell death via ferroptosis and caspase-1/GSDMD-dependent pyroptosis. And in vivo experiments confirmed that UCNP-Cro/FA upon NIR irradiation realized highly efficient

https://doi.org/10.1038/s41467-025-58124-7

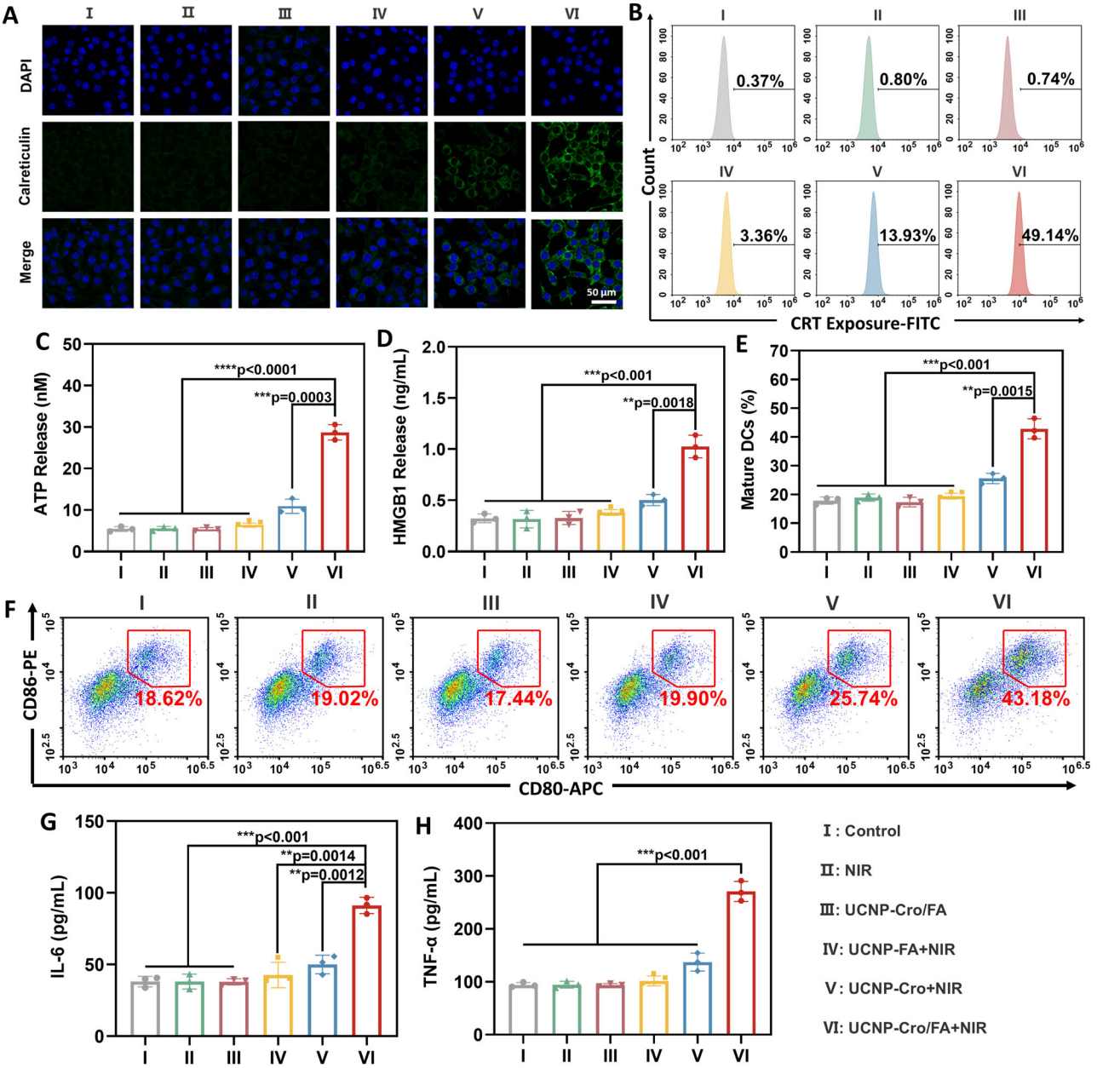

Fig. 8 | Induction of immunogenic cell death of 4T1 cells and in vitro DC maturation by UCNP-Cro/FA upon irradiation. A CLSM images of CRT exposure on 4T1 cells after different treatments. Scale bar=50 μm. **B** Flow cytometry analysis of CRT exposure on 4T1 cells after different treatments. **C**, **D** The level of extracellular secreted ATP (**C**) and HMGB1 (D) ($n = 3$ independent experiments in each group). Statistical significance was calculated using an unpaired two-tailed t-test. **E**, **F** Flow cytometry assay (**F**) and quantitative analysis (**E**) of in vitro DC maturation ($CD11c^+CD80^+CD86^+$) induced by 4T1 cells upon different treatments ($n = 3$ independent experiments in each group). Statistical significance was calculated using an unpaired two-tailed t-test. **G**, **H** IL-6 (**G**) and TNF-α (**H**) contents in the DC suspensions treated by 4T1 cells upon different treatments ($n = 3$ independent experiments in each group). Statistical significance was calculated using an unpaired two-tailed t-test. I: Control, II: NIR, III: UCNP-Cro/FA, IV: UCNP-FA + NIR, V: UCNP-Cro+NIR, VI: UCNP-Cro/FA + NIR. Experiments in (**A**), (**B**) and (**F**) were repeated three times independently with similar results. Error bars represent the mean ± SD. Source data are provided as a Source Data file.

antitumor therapy with little systemic toxicity. Additionally, the immunogenic pyroptosis and ferroptosis of tumor cells, along with M1 polarization of TAMs induced by UCNP-Cro/FA + NIR, collaboratively activated a potent anti-tumor immune response in immunocompetent mice model, offering preliminary evidence for the potential of UCNP-Cro/FA in advancing immunotherapeutic strategies. Considering the potential advantages of ferroptosis/pyroptosis therapy over conventional anticancer approaches, the dual-inductive nanosystem described herein emerges as a promising modality for antitumor treatment. Meanwhile, this study offered new insights into the engineering of nanoplatforms capable of mobilizing and hijacking endogenous iron for a safe and high-performance antitumor therapy.

Methods

Ethics Statement

All animal experiments were performed following the National Institutes of Health Guide for the Care and Use of Laboratory Animals with the approval of the Scientific Investigation Board of Zhejiang University, Hangzhou, China, under production license number ZJU20240568. According to the national and institutional guidelines,

https://doi.org/10.1038/s41467-025-58124-7

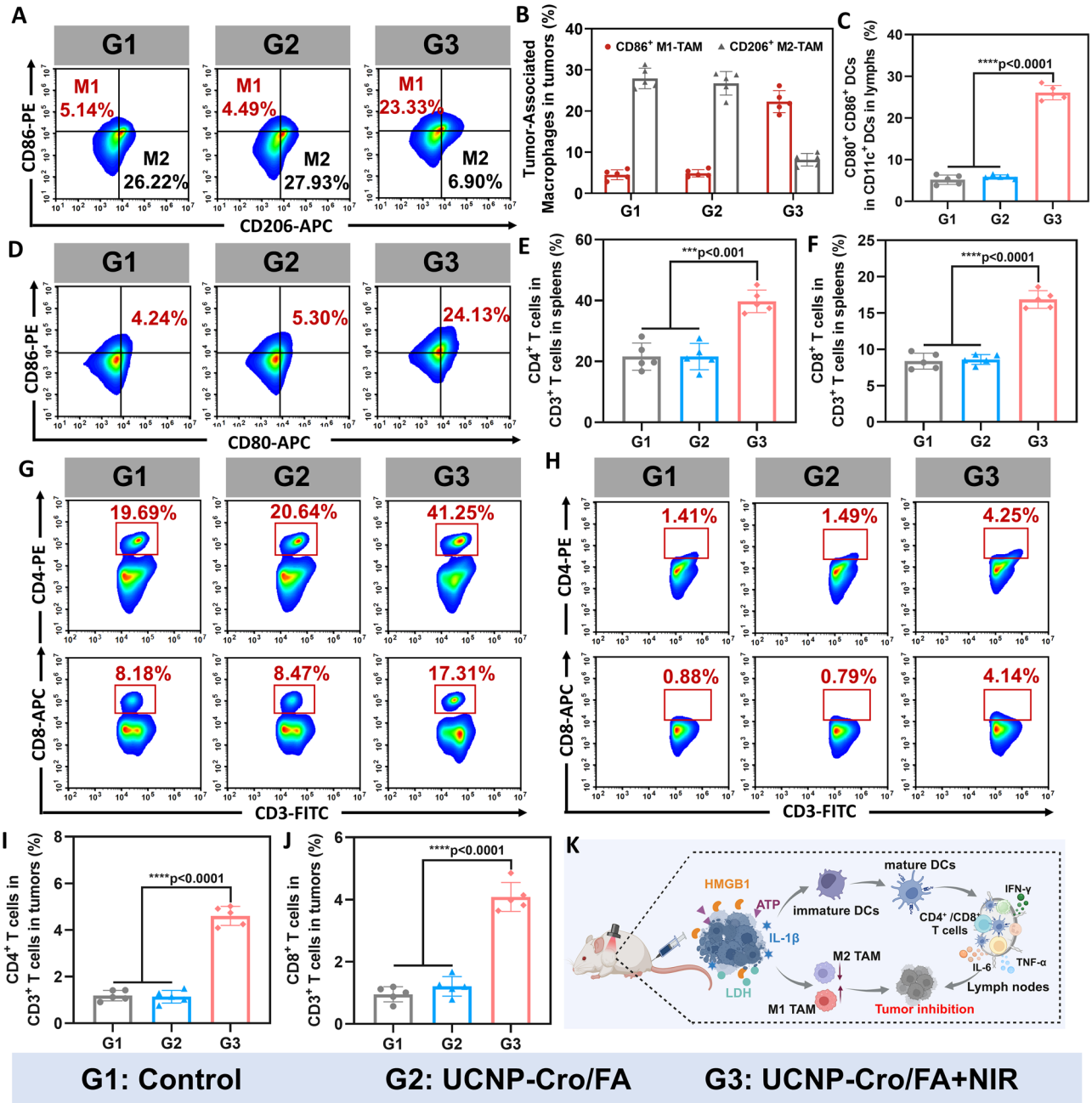

Fig. 9 | Activation of in vivo antitumor immune response by UCNP-Cro/FA upon irradiation. A, **B** Flow cytometric analysis (**A**) and quantification (**B**) of M1-type TAMs (F4/F80$^+$CD86$^+$) and M2-type TAMs (F4/F80$^+$CD206$^+$) in tumors of mice after different treatments ($n = 5$ mice in each group). Statistical significance was calculated using an unpaired two-tailed t-test. **C**, **D** Flow cytometric analysis (**D**) and quantification (**C**) of matured DCs (CD11c$^+$CD80$^+$CD86$^+$) in lymph nodes of mice after different treatments ($n = 5$ mice in each group). Statistical significance was calculated using an unpaired two-tailed t-test. **E**–**G** Flow cytometric analysis (**G**) and quantification of CD4$^+$ T cells (CD3$^+$CD4$^+$) (**E**), CD8$^+$ T cells (CD3$^+$CD8$^+$) (F) in spleens of mice after different treatments ($n = 5$ mice in each group). Statistical significance was calculated using an unpaired two-tailed t-test. **H**–**J** Flow cytometric analysis (**H**) and quantification of CD4$^+$ T cells (CD3$^+$CD4$^+$) (I), CD8$^+$ T cells (CD3$^+$CD8$^+$) (**J**) in tumors of mice after different treatments ($n = 5$ mice in each group). Statistical significance was calculated using an unpaired two-tailed t-test. **K** Mechanism of in vivo immune response activated by UCNP-Cro/FA upon irradiation. Created in BioRender. Luwen, Z. (2025) BioRender.com/m89r278. Groups 1, 2 and 3 represent Control, UCNP-Cro/FA and UCNP-Cro/FA + NIR, respectively. Error bars represent the mean ± SD. Source data are provided as a Source Data file.

the maximum tumor size allowed was 2000 mm^3, and there was on tumor burden exceeded the threshold.

Materials

Methyl isonipecotate, thiophene-2-thiol, croconic acid, $YCl_3{\cdot}6H_2O$, $YbCl_3{\cdot}6H_2O$, $TmCl_3{\cdot}6H_2O$, 2-aminoethyl dihydrogenphosphate (AEP), ammonium fluoride (NH_4F), sodium hydroxide (NaOH), $FeCl_3{\cdot}6H_2O$, ferrostatin-1 (Fer-1), 3-methyladenine (3-MA), acridine orange (AO) were purchased from Sigma-Aldrich (St. Louis, MO, USA). The iron assay kit was purchased from Dojindo (Tokyo, Japan). The BODIPY581/591-C11 probe and 3′-(p-hydroxyphenyl) fluorescein (HPF) probe were obtained from Thermo Fisher Scientific (Waltham, MA, USA). Anti-GPX4 antibody and anti-LC3 polyclonal antibody were obtained from Proteintech Group Inc. (Wuhan, China). Anti-Cathepsin B antibody, anti-ferritin antibody and anti-NCOA4 antibody were purchased from Abcam (Shanghai, China).

Cell lines and animals

Human breast cancer cells MCF-7 (FH0215) were purchased from FuHeng Biology (Shanghai,China). Mouse breast cancer cells 4T1 (CL-0007), human cervical cancer cells Hela (CL-0101), human lung cancer cells A549 (CL-0016), mouse monocyte-macrophage leukemia cells RAW264.7 (CL-0190) were purchased from Pricella Biotechnology (Wuhan, China). These cell lines were authenticated by Wuhan Pricella Biotechnology (Wuhan, China) using STR analysis. All cell lines were tested negative by using Myco-Lumi Luminescent Mycoplasma Detection Kit for mycoplasma contamination. MCF-7 cells, Hela cells, and macrophage RAW264.7 cells were separately cultured in DMEM medium containing 10% fetal bovine serum (FBS) and 1% streptomycin-penicillin. 4T1 cells were separately cultured in RPMI-1640 medium containing 10% FBS and 1% streptomycin-penicillin. A549 cells were cultured in Ham's F-12K medium containing 10% FBS and 1% streptomycin-penicillin. All cells were maintained at 37 °C in a humidified atmosphere with 5% CO_2 (Heraeus, Germany).

Female BALB/c nude mice (8 weeks, 20–25 g), and female BALB/c mice (6 weeks, 20–25 g) were obtained from Zhejiang Academy of Medical Sciences (Hangzhou, China). All animals were maintained at 22–23 °C, 45–55% relative humidity with a 12-12 h light-dark cycle with free food and water supplies. Findings do not apply to only one sex. Female mice were chosen due to males are aggressive to fight and usually get injured, which influences the data collection.

Synthesis and characterization of 2,5-bis[(4-carboxylic-piperidylamino)thiophenyl]- croconaine (Cro)

The croconaine dyes were synthesized in three steps. First, methyl isonipecotate (1.08 g, 7.5 mmol) was added to a solution containing thiophene-2-thiol (0.58 g, 5 mmol) in toluene (10 mL). After refluxed with stirring under nitrogen atmosphere for 2 h, the reaction mixture was cooled down to room temperature and further purified via column chromatography on silica gel, employing hexane and ethyl acetate (5:1, v/v) as the eluent. This process afforded the desired product, methyl 1-(thiophen-2-yl)piperidine-4-carboxylate, as a pale yellow solid with a yield of ~70%. ^{1}H NMR (600 MHz, $CDCl_3$): 6.78 (dd, 1H), 6.60 (dd, 1H), 6.13 (d, 1H), 3.71 (s, 3H), 3.52 (m, 2H), 2.83 (td, 2H), 2.44 (tt, 1H), 1.94 (m, 4H).

Then, above product (0.45 g, 2 mmol) was combined with 0.5 M sodium hydroxide solution (10 mL) and subjected to reflux conditions for 1 hour. the resulting solution was acidified with 10% acetic acid, resulting in the formation of a white precipitate. This precipitate was subsequently filtered and dried under vacuum to obtain 1-(thiophen-2-yl)piperidine-4-carboxylic acid (0.32 g, yield 76%).^{1}H NMR (600 MHz, $CDCl_3$): 6.71 (dd, 1H), 6.55 (dd, 1H), 6.07 (dd, 1H), 3.45 (m, 2H), 2.78 (td, 2H), 2.41 (tt, 1H), 1.91 (m, 4H).

Next, croconic acid (71 mg, 0.5 mmol) and 1-(thiophen-2-yl) piperidine-4-carboxylic acid (211 mg, 1 mmol) were introduced into a solution containing n-butanol and toluene (10 mL, 1:1, v/v), and reflux for 1 h. Upon cooling to room temperature, the resulting mixture underwent filtration, methanol washing, and vacuum drying to afford the pure product as black solid. (0.16 g, yield 61%). The structure of the product was identified using ^{1}H-NMR spectroscopy (AC-80, Bruker) in d_6-DMSO (Supplementary Fig. 4). The mass of the product was analyzed using ultraflex TOF/TOF mass spectrometry (Bruker), with mass spectra obtained in positive ESI mode in the range 0–1000 m/z (Supplementary Fig. 5).

Synthesis of Amino-Functionalized NaYF4: Yb^{3+}, Tm^{3+}UCNPs ($UCNP\text{-}NH_2$)

The NaYF4: 25%Yb, 0.5%Tm nanoparticles were synthesized via the thermal decomposition method. In particular, rare-earth sources of $YCl_3{\cdot}6H_2O$ (0.745 mmol), $YbCl_3{\cdot}6H_2O$ (0.25 mmol), $TmCl_3{\cdot}6H_2O$ (0.005 mmol) were mixed with oleic acid (6 mL) and 1-octadecene (15 mL) in a 100 mL three-neck round-bottom flask. The resulting mixture was heated up to 160 °C under argon protection with constant stirring for 1 h to form a homogeneous solution. When the temperature descended to 50 °C, a nucleation-inducing solution of NaOH (2.5 mmol) and NH_4F (4 mmol) in methanol (10 mL) was added to the flask. The reaction mixture was stirred for 30 min under a gentle argon flow and then heated to 120 °C for methanol extraction. After that, the solution was quickly heated to 305 °C and maintained for 1.5 h under argon atmosphere. At last, the products were precipitated from the solution with ethanol, repeatedly washed with ethanol/cyclohexane (9:1, v/v), and redispersed in cyclohexane.

The ligand exchange process was conducted to transfer hydrophobic $NaYF_4$: Tm^{3+}/Yb^{3+} UCNPs into aqueous-dispersible ones using 2-aminoethyl dihydrogenphosphate (AEP) as ligand. The cyclohexane solution of UCNPs was added dropwise to a solution of AEP (200 mg) in a mixture of deionized (DI) water and ethanol (3:2, v/v, 10 mL). After the mixture was vigorously stirred for 24 h at room temperature, the transfer of UCNPs was confirmed by the emission of the upper aqueous layer under 980 nm laser excitation. Following this, the AEP terminated UCNP ($UCNP\text{-}NH_2$) was allowed to be collected by centrifugation, washed three times, and redispersed in water for further use. And the amount of amine groups per milligram of UCNP was measured via fluorescamine assay using AEP as standard.

Construction of UCNP-Cro/FA

The FA–PEG-COOH (Mw=3400) and Cro was covalently linked with the $UCNP\text{-}NH_2$ to obtain Folic acid/Cro-modified UCNP (UCNP-Cro/FA). Briefly, FA-PEG-COOH (19.2 mg, 0.005 mmol) and Cro (5.3 mg, 0.01 mmol) was activated by EDC and NHS, and then reacted with $UCNPs\text{-}NH_2$ (65.8 mg, containing 0.01 mmol amine groups) for 24 h in the dark. The finial nanoconjugates (UCNP-Cro/FA) were collected by centrifugation and then washed with water. The Cro content attach to UCNPs was calculated according to the Cro concentration-absorbance correlation standard curve (Supplementary Fig. 6).

Detection of UCNP-Cro/FA chelation with Fe^{3+} ions

To assess the coordination capability of UCNP-Cro/FA towards Fe^{3+} ions, the UV-vis absorption spectra and fluorescence imaging of UCNP-Cro/FA solution after incubation with various concentrations of Fe^{3+} were investigated. $FeCl_3$ was dissolved in DI water to yield a stock solution (10 mM). Subsequent dilutions were performed to obtain different concentrations of Fe^{3+}, each of which was mixed with UCNP-Cro/FA solution (with an equivalent Cro concentration of 20 μM). Following ultrasonic treatment for 10 minutes, the absorption spectra were recorded within the range of 500 to 1000 nm, and fluorescence imaging of the solution (Ex/ Em=780 nm/820 nm) was conducted using an imaging system (IVIS Spectrum, Caliper, USA).

Near infrared (NIR)-to-UV-induced conversion of Fe^{3+} to Fe^{2+}

To investigate the transformation of Fe^{3+} to Fe^{2+} under NIR-to-UV conversion, the concentration of Fe^{2+} in the mixture of UCNP-Cro/FA and Fe^{3+} solution during 980 nm NIR irradiation was determined by the Fe-phenanthroline method. Fe^{2+} can form a stable complex with 1,10-phenanthroline, characterized by maximum absorbance at 510 nm. The absorbance of the complex supernatant was monitored using UV spectrophotometer (UV-2600, SHIMADZU, Japan). Specifically, 1,10-phenanthroline (0.06 wt%) was incorporated into the UCNP-Cro/FA (500 ug/mL) and Fe^{3+} (20 μM) solution mixture, followed by exposure to a 980 nm laser. After incubation for 10 min, alterations in the UV absorbance of the solutions were recorded at different times.

Besides, analysis was also conducted on the UV-vis absorption spectra and fluorescence imaging of the mixed solution, composed of UCNP-Cro/FA and Fe^{3+}, subsequent to irradiation.

Subcellular localization analysis

To track the colocation of nanoformulations and lysosomes, MCF-7 cells were incubated with UCNP-Cro and UCNP-Cro-FA nanoparticles

for 4 h, respectively. Subsequently, Lyso-Tracker Green (50 nM) was added to label lysosomes in the cells and incubated for 30 min at 37 °C. After that, the cells were washed twice with cold PBS, followed by fixing with 4 % paraformaldehyde and staining nuclei using DAPI for 15 min. Finally, the cells were visualized by CLSM (Lyso-Tracker Green, Ex/Em = 488 nm/500–550 nm).

Intracellular Fe^{2+} ions content detection

FeRhoNox-1, functioning as an intracellular Fe^{2+} ion indicator, can penetrate the cell membrane and react with Fe^{2+} ions to yield orange fluorescent products. After MCF-7 cells were incubated with UCNP-FA, UCNP-Cro or UCNP-Cro/FA nanoparticles (400 μg/mL corresponding to Cro concentration: 12.8 μg/mL) in 12-well plates for 12 h, fresh serum-free medium containing FeRhoNox-1 (5 μM) was substituted for the old medium. The cells were incubated for an additional 1 h and then examined by CLSM and FCM. (FeRhonox-1, Ex/Em=530 nm/550–610 nm).

Ferritinophagy detection

To investigate the occurrence of nuclear receptor coactivator 4 (NCOA4)-mediated ferritinophagy, we assessed the expression levels of related proteins including light chain 3 (LC3), NCOA4, ferritin heavy chain (FTH).

immunofluorescence analysis was applied to detect the LC3 expression, which is a well-established marker for autophagosome formation. MCF-7 cells were plated in 6-well plates with cover glass and treated with UCNP-FA, UCNP-Cro and UCNP-Cro/FA nanoparticles (400 μg/mL) for an additional 12 h. After washing with PBS, the cells were fixed in 4% paraformaldehyde and permeabilized using 0.1% Triton X-100 for 5 min. Then, the cells were incubated with blocking buffer (5% BSA) for 1 h at room temperature. Following this, LC3 protein was labeled separately with Rabbit anti-LC3 polyclonal antibody (1:500, 14600-1-AP) and Alexa Fluor®488 goat anti-rabbit secondary antibody from Proteintech. The imaging of cells was recorded by CLSM. The expression levels of NCOA4 and FTH1 were analyzed by western blotting. Primary antibodies utilized were anti-NCOA4 (1:1000, E8H8Z) from Cell Signaling Technologies and anti-FTH (1:1000, A19544) from ABclonal Technology.

Lysosomal damage assay

Acridine orange (AO) staining assay was performed to test the integrity of Lysosomes. MCF-7 cells were treated with different formulations (UCNP-FA, UCNP-Cro and UCNP-Cro/FA nanoparticles; 400 μg/mL) and incubated for 12 h. Subsequently, NIR irradiation (980 nm, 1 W/cm^2, 10 min) was performed in those light-involved groups. After incubated for another 4 h, the cells in corresponding groups were stained by AO (5 μM) for 15 min. The imaging of cells was recorded by CLSM (Ex = 488 nm, Em = 500–550 nm (AO green fluorescence) and 610–640 nm (AO red fluorescence).

To ascertain the translocation of cathepsin B (CTSB) from lysosomes into cytosol, the cytosolic as well as lysosomal fractions of differently treated MCF-7 cells were prepared using a Lysosome Enrichment Kit (Bestbio, Shanghai, China) following the manufacturer's instructions. Briefly, harvested cells were resuspended in Lysosome Isolation Reagent A and gently oscillated on ice for 10 minutes. Subsequently, the cells were homogenized 30–40 times using a homogenizer. After two centrifugation steps (3000 g for 10 minutes followed by 20000 g for 20 minutes), the resulting supernatant was collected and labeled as cytosolic fraction. Meanwhile, the precipitation was resuspended with Lysosome Isolation Reagent B and centrifuged at 20000 g for 20 min. after removal of the supernatant, The obtained precipitate was further suspended with lysosome separation reagent C and oscillated on ice for 20 min. Finally, the lysis underwent centrifugation at 12000 g for 20 min to isolate a supernatant enriched in total lysosomal proteins. The levels of CTSB protein in the different fractions were then evaluated by western blot analysis. Primary antibodies utilized were anti-Cathepsin B (1:1000, D1C7Y) and anti-β-actin (1:1000, 13E5) from Cell Signaling Technologies, anti-LAMP1 (1:1000, 21997-1-AP) from Proteintech,.

Western blot analysis

For western blots of GPX4, cleaved caspase-1, cleaved gasdermin D and NLRP3, MCF-7 cells were incubated with UCNP-FA, UCNP-Cro and UCNP-Cro/FA nanoparticles (400 μg/mL) in 6-well plates for 12 h. After washing with PBS, the cells were treated with or without NIR irradiation (980 nm, 1 W/cm^2, 10 min) and further incubated for 6 h. Then the treated cells were collected and lysed to perform a standard western blot process according to the procedure described above. Primary antibodies utilized were anti-cleaved gasdermin D (1:500, Asp276), anti-cleaved caspase-1 (1:1,000, Asp297), and anti-NLRP3 (1:1000, D4D8T) from Cell Signaling Technologies, anti- GPX4 (1:2000, A11243) from ABclonal Technology.

Interleukin-1β (IL-1β) and Lactic dehydrogenase (LDH) release measurement

The release of IL-1β and LDH were detected by the IL-1β enzyme-linked immunosorbent assay (ELISA) kit (Meimian, MM-0181H2) and the LDH cytotoxicity assay kit (Beyotime, C0016), respectively, according to the manufacturer's instructions. MCF-7 cells were seeded into 96-well plates and then incubated with different formulations (UCNP-FA, UCNP-Cro and UCNP-Cro/FA nanoparticles; 400 μg/mL) for 12 h. After washing with PBS, cells in irradiation-involved groups were treated with NIR laser (980 nm, 1 W/cm^2, 10 min) and further incubated for 24 h. Lastly, the cell culture media were Centrifuged at 1000 g for 10 minutes to remove debris and the supernatants were collected for assay. For LDH detection, the cell supernatant (120 μL) was co-incubated with working fluid (60 μL) for 30 min. The optical absorbance at 490 nm was recorded using a microplate reader (Varioskan Flash, Thermo Scientific). For IL-1β detection, colorimetric absorption analysis was measured at 450 nm.

Cell morphology observation

MCF-7 cells were seeded in 24-well plates and exposed to various treatments (control, NIR alone, UCNP-Cro/FA NPs, UCNP-FA NPs+ NIR, UCNP-Cro NPs+NIR, and UCNP-Cro/FA NPs+NIR (NPs: 400 μg/mL). The morphology of cells was photographed by a light microscope. (IX-71, OLYMPUS, Japan).

For Scanning Electron Microscopy (SEM), the treated cells were fixed with 2.5% glutaraldehyde and 1% osmium tetroxide. After being dehydrated and dried, the specimens were mounted on stubes and sputter-coated with gold–palladium. The images were monitored by SEM (TM-3000, HITACHI, Japan).

siRNA transfection

siRNA sequences targeting GSDMD were synthesised by Servicebio Co., Ltd. MCF-7 cells were transfected with siRNA at a concentration of 50 nmol/L for 6 h using Lipofectamine 2000 transfection reagent (Thermo Fisher Scientific, MA, United States), after which the medium was changed into DMEM medium containing 10% FBS. Subsequently, GSDMD knockdown efficiency were confirmed by Western blot and quantitative real-time PCR before proceeding to subsequent experiments. Sequences of siRNAs were: siGSDMD: GGU GAA CAU CGG AAA GAU UTT (sense), AAU CUU UCC GAU GUU CAC CTT (antisense). Negative control siRNA (siNC): UUC UCC GAA CGA GUC ACG UTT (sense), ACG UGA CAC GUU CGG AGA ATT (antisense).

In vivo tumor targeting evaluation

To investigate the biodistribution of the nanoparticles, an MCF-7 tumor-bearing mouse model was established by subcutaneously injecting MCF-7 cells (1×10^6 suspended in 20 μL PBS) into the first

mammary pad of each BALB/c nude mouse (female, 8 weeks old, 20–25 g). After the tumor volume reached about 300 mm^3, the mice were randomized into the three groups and were intravenously injected with UCNP-Cro NPs, UCNP-Cro/FA NPs or UCNP-ICG/FA NPs at an equivalent ICG and Cro dose of 1 mg/kg. Subsequently, the fluorescence imaging of the whole-body was captured at 2, 4, 8, 12, and 24 h postinjection by an in vivo imaging system (IVIS Spectrum, Caliper, USA). At the end of the study, all mice were sacrificed, and the tumors and major organs were excised for ex vivo imaging. In addition, samples of tumor were digested in a mixture of aqua regia, and the UCNP contents were measured by ICP-OES (PerkinElmer, USA).

Tumor tissue Fe^{2+} and Ferritin level detection

The UCNP-Cro, UCNP-ICG/FA and UCNP-Cro/FA (ICG and Cro concentration of 1 mg/kg) were intravenously injected three times through the tail vein (day 0, 2 and 4). On day 5, all mice were sacrificed and the tumors were collected for analysis. To quantify the Fe^{2+} content, tumors were homogenized in 1 mL of ice-cold PBS, followed by centrifugation at 16000 g for 10 minutes at 4 °C. The levels of Fe^{2+} in the resulting supernatants were determined using Iron Assay Kits (Dojindo, Tokyo, Japan) according to the manufacture's instruction. Additionally, the harvested tumors were formalin-fixed, paraffin-embedded and sectioned, followed by immunohistochemistry staining with anti-ferritin monoclonal antibody (1:100) to detect the changes of ferritin levels within tumor tissues. All sections were visualized under the microscope and images were taken. Images were analyzed by the IHC profiler in ImageJ software to calculate the IHC score of each group based on randomly selected ten images. Briefly, IHC score is based on the average grey value of positive cells (staining intensity) and the percentage of positive area (staining area) in IHC images. The IHC scores include High Positive scores 4, Positive scores 3, Low Positive scores 2 and negative scores 1.

In vivo antitumor efficiency evaluation

MCF-7 cells (5×10^7 cells/mL) were orthotopically injected into the right first mammary pad of BALB/c nude mice (female, 8 weeks old, 20–25 g). As the tumor reached 50–60 mm^3, the mice were randomized into the following six groups: (1) PBS; (2) NIR; (3) UCNP-Cro/FA NPs; (4) UCNP-FA NPs + NIR; (5) UCNP-Cro + NIR; and (6) UCNP-Cro/FA NPs + NIR. The UCNP-FA, UCNP-Cro and UCNP-Cro/FA (200 μL, 5 mg/mL of UCNPs equivalent to 0.16 mg/mL Cro) were intravenously injected three times through the tail vein (day 0, 2 and 4). after 24 h post injection, each light exposure group was treated with 980 nm irradiation (2 W/cm^2) for 10 min, while the other groups did not. The tumor volume and body weights of mice was continuously measured every 2 days. On day 21, the tumors were excised for weighing and imaging. To examine the histopathologic toxicity, the harvested tumors and major organs (heart, liver, spleen, lung, and kidney) were sectioned for hematoxylin and eosin (H&E) staining. Moreover, the sectioned tumors were stained with anti-GPX4 and anti-Cleaved caspase-1 antibodies for immunohistochemical analysis and a terminal deoxynucleotidyl transferase-mediated deoxyuridine triphosphate nick-end labeling (TUNEL) assay for immunofluorescence.

In vitro dendritic cell (DC) stimulation

Bone marrow-derived DCs were derived from the bone marrow of BALB/c mice according to an established method. Immature DCs were cocultured with different nanoformulations-treated 4T1 cells using a Transwell system. Specifically, 4T1 cells were seeded in the upper chamber of a 24-well plate, while immature DCs were seeded in the lower chamber. Following laser irradiation or no treatment, the upper Transwell chambers were inserted in the lower chamber that contained immature DCs and incubated for an additional 24 h. Later, flow cytometry analysis was performed to detect the levels of CD11c, CD80, and CD86 for evaluating the maturation of DCs. Moreover, the supernatants were collected, and the secretion of IL-6 and TNF-α was quantified using ELISA kits.

Polarization of macrophages evaluation

RAW 264.7 cells were seeded in 6-well plates (4×10^5/well). After attachment, the old medium was replaced with a medium containing interleukin-4 (IL-4) (50 ng/mL) for 24 h to obtain M2-type macrophages. Then, the M2-type macrophages after being treated with NIR, UCNP-Cro/FA, UCNP-FA + NIR, UCNP-Cro+NIR, and UCNP-Cro/FA + NIR, were examined using RT-PCR assays and flow cytometry to assess the extent of macrophage repolarization.

In vivo antitumor immunity studies

To establish the 4T1 tumor-bearing Balb/c mouse model, 20 μL 1×10^6 4T1 cells were injected subcutaneously into each Balb/c mouse (female, 6 weeks old, 20–25 g), when the tumor grew to about 200 mm^3, the mice were randomly divided into 3 groups at 5 mice per group and subjected to different treatment (PBS, UCNP-Cro/FA, UCNP-Cro/FA + NIR). After 18 days of treatment, all mice were sacrificed, their tumor tissues, spleens and lymph nodes were collected for post-analysis:

For the assessment of TAMs polarization, tumors from three groups ($n = 5$) of mice were collected, ground in PBS, filtered and centrifuged to obtain single cell suspensions and supernatants. Tumor cell suspensions were then stained with corresponding antibodies, followed by phenotypic analysis of TAMs by FCM.

For DCs maturation analysis, lymph nodes were collected from three groups ($n = 5$) of mice and single cell suspensions were obtained by grinding and filtering in PBS. The cell suspensions of lymph nodes were then stained with corresponding antibodies for DCs maturation analysis by FCM.

For T cells activation, spleens and tumors were collected from three groups ($n = 5$) of mice, single cell suspensions and supernatants were obtained by grinding and filtration centrifugation in PBS. Additionally, single-cell suspensions were washed with erythrocyte lysis buffer to eliminate erythrocytes. The splenocyte and tumor cell suspensions were then stained with the appropriate antibodies and evaluated using FCM. Meanwhile, the levels of cytokines in tumor cell suspensions were measured using ELISA kits.

Statistical analysis

Data were represented as mean ± standard error. Statistical analyses, including unpaired or paired student's t-tests for comparisons between two or several groups, were conducted as appropriate. Prism software version 8.0 (GraphPad) was employed to perform all statistical analyses, with a value of $P < 0.05$ considered to be statistically significant.

Reporting summary

Further information on research design is available in the Nature Portfolio Reporting Summary linked to this article.

Data availability

The analysis results of mass spectrometry and NMR are included in Supplementary Figs. 2–5, and the raw data are included in source data file with the tab names of Supplementary Figs. 2–4 and Supplementary Fig. 5, respectively. All other data supporting the findings of the paper are available in the article, supplementary information or source data file. Source data are provided with this paper.

References

1. Siegel, R. L., Giaquinto, A. N. & Jemal, A. Cancer statistics, 2024. *CA-Cancer J. Clin.* **74**, 12–49 (2024).
2. Obidiro, O., Battogtokh, G. & Akala, E. O. Triple negative breast cancer treatment options and limitations: future outlook. *Pharmaceutics* **15**, 1796 (2023).

3. Tohme, S., Simmons, R. L. & Tsung, A. Surgery for cancer: a trigger for metastases. *Cancer Res* **77**, 1548–1552 (2017).
4. Ferrari, P. et al. Molecular mechanisms, biomarkers and emerging therapies for chemotherapy resistant TNBC. *Int. J. Mol. Sci.* **23**, 1665 (2022).
5. Zhou, Q. et al. Ferroptosis in cancer: from molecular mechanisms to therapeutic strategies. *Signal Transduct. Target. Ther.* **9**, 55 (2024).
6. Yu, P. et al. Pyroptosis: mechanisms and diseases. *Signal Transduct. Target. Ther.* **6**, 128 (2021).
7. Wang, Y. et al. Cuproptosis: a novel therapeutic target for overcoming cancer drug resistance. *Drug Resist. Update* **72**, 101018 (2024).
8. Xu, R. et al. Ferroptosis/pyroptosis dual-inductive combinational anti-cancer therapy achieved by transferrin decorated nanoMOF. *Nanoscale Horiz.* **6**, 348–356 (2021).
9. Wang, S. et al. Combination of ferroptosis and pyroptosis dual induction by triptolide nano-MOFs for immunotherapy of Melanoma. *J. Nanobiotechnol.* **21**, 383 (2023).
10. Dixon, S. J. et al. Ferroptosis: an iron-dependent form of non-apoptotic cell death. *Cell* **149**, 1060–1072 (2012).
11. Nakamura, K. et al. Activation of the NLRP3 inflammasome by cellular labile iron. *Exp. Hematol.* **44**, 116–124 (2016).
12. Zhou, B. et al. Tom20 senses iron-activated ROS signaling to promote melanoma cell pyroptosis. *Cell Res.* **28**, 1171–1185 (2018).
13. Liu, Y. et al. Liposomes embedded with PEGylated iron oxide nanoparticles enable ferroptosis and combination therapy in cancer. *Natl Sci. Rev.* **10**, nwac167 (2023).
14. Xie, B. et al. Supramolecularly engineered conjugate of bacteria and cell membrane-coated magnetic nanoparticles for enhanced ferroptosis and immunotherapy of tumors. *Adv. Sci.* **10**, e2304407 (2023).
15. Liu, H. et al. Biodegradable amorphous copper iron tellurite promoting the utilization of fenton-like ions for efficient synergistic cancer theranostics. *ACS Appl. Mater. Interfaces* **14**, 28537–28547 (2022).
16. Liang, H. et al. Renal clearable ultrasmall single-crystal Fe nanoparticles for highly selective and effective ferroptosis therapy and immunotherapy. *J. Am. Chem. Soc.* **143**, 15812–15823 (2021).
17. Lin, L. et al. Endogenous labile iron pool-mediated free radical generation for cancer chemodynamic therapy. *J. Am. Chem. Soc.* **142**, 15320–15330 (2020).
18. Guan, Q., Zhou, L. L. & Dong, Y. B. Ferroptosis in cancer therapeutics: a materials chemistry perspective. *J. Mater. Chem. B* **9**, 8906–8936 (2021).
19. Rizzollo, F., More, S., Vangheluwe, P. & Agostinis, P. The lysosome as a master regulator of iron metabolism. *Trends Biochem. Sci.* **46**, 960–975 (2021).
20. Ma, S., Henson, E. E., Chen, Y. & Gibson, S. B. Ferroptosis is induced following siramesine and lapatinib treatment of breast cancer cells. *Cell Death Dis.* **7**, e2307 (2016).
21. Antoszczak, M. et al. Iron-sensitive prodrugs that trigger active ferroptosis in drug- tolerant pancreatic cancer cells. *J. Am. Chem. Soc.* **144**, 11536–11545 (2022).
22. Xiong, H., Wang, C., Wang, Z. H., Lu, H. P. & Yao, J. Self-assembled nano-activator constructed ferroptosis-immunotherapy through hijacking endogenous iron to intracellular positive feedback loop. *J. Control. Release* **332**, 539–552 (2021).
23. Li, W. et al. Molecular engineering of pH-Responsive NIR oxazine assemblies for evoking tumor ferroptosis via triggering lysosomal dysfunction. *J. Am. Chem. Soc.* **145**, 3736–3747 (2023).
24. Ye, T. et al. Lysosomal destabilization: a missing link between pathological calcification and osteoarthritis. *Bioact. Mater.* **34**, 37–50 (2024).
25. Wang, J. et al. Cathepsin B aggravates acute pancreatitis by activating the NLRP3 inflammasome and promoting the caspase-1-induced pyroptosis. *Int. Immunopharmacol.* **94**, 107496 (2021).
26. Zhang, H. et al. Co-exposure of chronic stress and alumina nanoparticles aggravates hippocampal microglia pyroptosis by activating cathepsin B/NLRP3 signaling pathway. *J. Hazard. Mater.* **436**, 129093 (2022).
27. You, Y. et al. A photo-activable nano-agonist for the two-signal model of T cell in vivo activation. *J. Control. Release* **361**, 681–693 (2023).
28. Wang, S., Cong, T. T., Liang, Q., Li, Z. Y. & Xu, S. Dual colorimetric and fluorescent chemosensor of Fe3+ and Cu2+ based on 2,5-bis[(4-carboxylic-piperidylamino)thiophenyl]-croconine. *Tetrahedron* **71**, 5478–5483 (2015).
29. Zeng, F. et al. Coordinating the mechanisms of action of ferroptosis and the photothermal effect for cancer theranostics. *Angew. Chem. Int. Ed. Engl.* **61**, e202112925 (2022).
30. Sun, R. et al. pH-activated nanoplatform for visualized photodynamic and ferroptosis synergistic therapy of tumors. *J. Control. Release* **350**, 525–537 (2022).
31. Bao, W. E. et al. Nanolongan with multiple on-demand conversions for ferroptosis-apoptosis combined anticancer therapy. *ACS Nano* **13**, 260–273 (2019).
32. Nguyen, N. T. et al. Amplified Fenton-based oxidative stress utilizing ultraviolet upconversion luminescence-fueled nanoreactors for apoptosis-strengthened ferroptosis anticancer therapy. *ACS Nano* **17**, 382–401 (2023).
33. Scaranti, M., Cojocaru, E., Banerjee, S. & Banerji, U. Exploiting the folate receptor α in oncology. *Nat. Rev. Clin. Oncol.* **17**, 349–359 (2020).
34. Bao, W. et al. MOFs-based nanoagent enables dual mitochondrial damage in synergistic antitumor therapy via oxidative stress and calcium overload. *Nat. Commun.* **12**, 6399 (2021).
35. Movileanu, C. et al. Folic acid-decorated PEGylated magnetite nanoparticles as efficient drug carriers to tumor cells overexpressing folic acid receptor. *Int. J. Pharm.* **625**, 122064 (2022).
36. Galy, B., Conrad, M. & Muckenthaler, M. Mechanisms controlling cellular and systemic iron homeostasis. *Nat. Rev. Mol. Cell Biol.* **25**, 133–155 (2024).
37. Chen, Y. et al. Boosting ROS-mediated lysosomal membrane permeabilization for cancer ferroptosis therapy. *Adv. Healthc. Mater.* **12**, e2202150 (2023).
38. Chen, B. et al. A pyroptosis nanotuner for cancer therapy. *Nat. Nanotechnol.* **17**, 788–798 (2022).
39. Balasubramanian, A. et al. The palmitoylation of gasdermin D directs its membrane translocation and pore formation during pyroptosis. *Sci. Immunol.* **9**, eadn1452 (2024).
40. Li, Y. et al. Tumor Microenvironment-responsive yolk-shell NaCl@-Virus-inspired tetrasulfide-organosilica for ion-interference therapy via osmolarity surge and oxidative stress amplification. *ACS Nano* **16**, 7380–7397 (2022).
41. Deng, H. Z. et al. Chemodynamic and photothermal combination therapy based on dual-modified metal-organic framework for inducing tumor ferroptosis/pyroptosis. *ACS Appl. Mater. Interfaces* **14**, 24089–24101 (2022).
42. Liu, J. P. et al. Ultrathin Clay nanoparticles-mediated mutual reinforcement of ferroptosis and cancer immunotherapy. *Adv. Mater.* **36**, e2309562 (2024).
43. Ding, B. B. et al. Sodium bicarbonate nanoparticles for amplified cancer immunotherapy by inducing pyroptosis and regulating lactic acid metabolism. *Angew. Chem. Int. Ed.* **62**, e202307706 (2023).
44. Xu, X. Y. et al. Bioorthogonal/ultrasound activated oncolytic pyroptosis amplifies tumor vaccination for boosting antitumor immunity. *ACS Nano* **18**, 9413–9430 (2024).
45. Puig-Kröger, A. et al. Folate receptor β is expressed by tumor-associated macrophages and constitutes a marker for M2 anti-inflammatory/regulatory macrophages. *Cancer Res.* **69**, 9395–9403 (2009).

46. Cresswell, G. M. et al. Folate receptor beta designates immunosuppressive tumor-associated myeloid cells that can be reprogrammed with folate-targeted drugs. *Cancer Res.* **81**, 671–684 (2021).
47. Mu, Q. D. et al. The role of iron homeostasis in remodeling immune function and regulating inflammatory disease. *Sci. Bull.* **66**, 1806–1816 (2021).

Acknowledgements

This work did not receive any specific grant from funding agencies in the public, commercial, or not-for-profit sectors.

Author contributions

L.M.W., Y.Z.D., C.X.Z., and B.T. designed and guided the overall research project. L.W.Z. performed the experiments and wrote the original draft and review & editing. J.H.H. assisted with animal experiments. X.C.W. and J.C.Z. involved the data analysis and other property characterizations. X.Y.X. and X.J.H. provided intellectual input and helped interpret the results.

Competing interests

The authors declare no competing interests.

Additional information

Supplementary information The online version contains supplementary material available at https://doi.org/10.1038/s41467-025-58124-7.

Correspondence and requests for materials should be addressed to Bing Tian, Chun-Xia Zhao, Yongzhong Du or Liming Wu.

Peer review information *Nature Communications* thanks Kohsuke Tsuchiya and the other, anonymous, reviewer(s) for their contribution to the peer review of this work. A peer review file is available.